Cell Reports
Article

The Amyloid Precursor Protein C-Terminal Domain Alters CA1 Neuron Firing, Modifying Hippocampus Oscillations and Impairing Spatial Memory Encoding

Paula A. Pousinha,[1,5,*] Xavier Mouska,[1] Daniela Bianchi,[2] Mariana Temido-Ferreira,[3] Joana Rajão-Saraiva,[3] Rui Gomes,[3] Sebastian P. Fernandez,[1] Ana Rita Salgueiro-Pereira,[1] Carine Gandin,[1] Elisabeth F. Raymond,[1] Jacques Barik,[1] Romain Goutagny,[4] Ingrid Bethus,[1] Luisa V. Lopes,[3] Michele Migliore,[2] and Hélène Marie[1]

[1]Université Côte d'Azur, CNRS UMR 7275, IPMC, Valbonne, France
[2]Institute of Biophysics, National Research Council, Palermo, Italy
[3]Instituto de Medicina Molecular, Faculdade de Medicina de Lisboa, Universidade de Lisboa, Lisboa, Portugal
[4]Université de Strasbourg, CNRS UMR 7364, LNCA, Strasbourg, France
[5]Lead Contact
*Correspondence: pousinha@ipmc.cnrs.fr
https://doi.org/10.1016/j.celrep.2019.08.103

SUMMARY

There is a growing consensus that Alzheimer's disease (AD) involves failure of the homeostatic machinery, which underlies the firing stability of neural circuits. What are the culprits leading to neuron firing instability? The amyloid precursor protein (APP) is central to AD pathogenesis, and we recently showed that its intracellular domain (AICD) could modify synaptic signal integration. We now hypothesize that AICD modifies neuron firing activity, thus contributing to the disruption of memory processes. Using cellular, electrophysiological, and behavioral techniques, we show that pathological AICD levels weaken CA1 neuron firing activity through a gene-transcription-dependent mechanism. Furthermore, increased AICD production in hippocampal neurons modifies oscillatory activity, specifically in the γ-frequency range, and disrupts spatial memory task. Collectively, our data suggest that AICD pathological levels, observed in AD mouse models and in human patients, might contribute to progressive neuron homeostatic failure, driving the shift from normal aging to AD.

INTRODUCTION

Alzheimer's disease (AD) is an incurable neurodegenerative disorder, with increasing prevalence in aging populations. Almost two decades ago, Selkoe (2002) convincingly proposed that AD begins with subtle alterations at the synapse leading to synaptic failure. Yet, could synaptic modifications alone account for the collapse of neural networks stability? Currently, there is a growing consensus that AD results from the failure of the homeostatic machinery, which underlies the firing stability of neural circuits, hence precipitating an imbalance between neuron firing stability and synaptic plasticity (De Strooper and Karran, 2016; Frere and Slutsky, 2018). Indeed, whole-head magnetoencephalography (MEG) studies show alterations in firing synchronization at gamma (30–80 Hz) frequencies in AD patients and AD mouse models (Gillespie et al., 2016; Palop et al., 2007; Stam et al., 2002; Verret et al., 2012). The molecular mechanisms underlying these neuron firing modifications remain to be clearly elucidated.

Human genetic evidence indicates that the amyloid precursor protein (APP) is central to the pathogenesis of AD (Jonsson et al., 2012; van der Kant and Goldstein, 2015). Comprehensive characterization of mutant APP-overexpressing transgenic mice have reported changes of firing homeostasis in both excitatory and inhibitory neurons of the hippocampus (Brown et al., 2011; Hazra et al., 2013; Kaczorowski et al., 2011; Kerrigan et al., 2014; Minkeviciene et al., 2009; Wykes et al., 2012), the entorhinal cortex (Marcantoni et al., 2014), the cortex (Hazra et al., 2013; Verret et al., 2012), and the cerebellum (Hoxha et al., 2012), but the entities behind these firing modifications are yet to be identified. In these models, the contribution of individual peptides generated from abnormal or enhanced proteolytic APP cleavage cannot be dissociated. Approaches allowing to decipher the contribution of individual APP fragments to the modulation of neuron firing, are thus needed and will be crucial to fully understand the complexity of AD pathogenesis.

We and others have shown that the APP intracellular domain (AICD) is increased in the brain of AD patients and animal models (Ghosal et al., 2009; Lauritzen et al., 2012; Pousinha et al., 2017). Given its impact on nuclear signaling (Bukhari et al., 2017), AICD stands as a key APP fragment to shape cellular functions. Of note, this APP fragment has been linked to the neuron homeostatic machinery as AICD was shown to modulate intracellular calcium homeostasis (Hamid et al., 2007; Leissring et al., 2002), and destabilization of intracellular calcium is a key factor leading to neuronal intrinsic excitability disruption (Zhang and Linden, 2003). Notably, both AICD lack of expression (Ghosal et al., 2009; Klevanski et al., 2015) and overexpression (Ghosal et al., 2009) lead to memory deficits. Together, these data suggest that an imbalance in AICD levels, and therefore function, has detrimental cellular impact and could thus contribute to AD

pathogenesis. We here asked whether pathological levels of AICD could affect neuron firing and oscillatory activity, thus contributing to the disruption of memory processes.

RESULTS

AICD Weakens CA1 Pyramidal Neuron Firing in the γ Frequency Range through a Gene-Transcription-Dependent Mechanism

First, we examined the impact of AICD on neuron firing activity. We increased intracellular AICD levels by using *in vivo* transduction of neurotropic recombinant adeno-associated viruses (AAVs) encoding AICD (Figures 1A and 1B), as described in detail in Pousinha et al. (2017). Briefly, the human AICD c-DNA sequence (last 50 amino acids of APP) was inserted in an AAV vector also expressing GFP (called hereafter AICD virus). We also created AAVs expressing AICD coupled to a nuclear localization signal (NLS) (AICD^{nls} virus) or coupled to a nuclear exporting signal (NES) (AICD^{nes} virus) to allow discrimination between the nuclear versus cytoplasmatic roles of AICD. The AAV vector expressing only GFP was used as control (GFP virus) (Figure S1A). Whole-cell current-clamp recordings of CA1 pyramidal cells transduced with different virus (AICD, AICD^{nls}, AICD^{nes}, and GFP) were performed (Figures 1A and 1B). No alterations were observed regarding the resting membrane potential (Figure S1B), nor the membrane input resistance (Figures S1C–S1E). In order to study supra-threshold CA1 pyramidal cells properties in the transduced neurons, 200-ms depolarizing current pulses, incrementing in steps of 50 pA, were applied at a pre-stimulus potential fixed at −65 mV and AP firing properties were analyzed (Figure 1C). As illustrated (Figure 1D), when a current injection of 300 pA was applied, AICD or AICD^{nls} neurons fired at a lower frequency than GFP or AICD^{nes} neurons, a difference that was systematically observed for current injections higher than 300 pA. Thus, increased levels of AICD disrupt firing activity at the gamma-frequency range. Moreover, this effect likely requires AICD presence in the nucleus as neurons transduced with AICD^{nes} behaved like GFP neurons.

Spike-frequency adaptation is a property of many neurons defined as a decreasing rate of action potential (AP) firing during prolonged excitation. This mechanism has been shown to play roles in perceptual processing and learning (Benda et al., 2005; Moyer et al., 2000; Peron and Gabbiani, 2009). To better evaluate the ability of AICD neurons to adapt their firing behavior with time, we measured the firing adaptation ratio for I = 500 pA in the transduced neurons. As shown (Figure 1E), AICD or AICD^{nls} neurons present higher firing adaptation than GFP neurons (~40% higher). Importantly, AICD^{nes} neurons showed similar firing adaptation ratio to GFP neurons pointing again for a nuclear role of AICD in this phenotype. Further analysis of AP shape and AP adaptation was performed in order to access the cellular mechanism linked to the AICD effect on neuron intrinsic excitability. Using phase-plane plots of dV/dt versus V for the first and last APs of trains generated during 500-pA current steps (Figure S2), we estimated the average dV/dt_{max} as an indication of the maximal Na^+ current contributing to the AP (Colbert et al., 1997; Marcantoni et al., 2014) and the voltage at which dV/dt_{max} is 4% of its maximum as the threshold potential of AP generation (Bean, 2007). As shown in Figure S2, these parameters were similar in GFP, AICD, and AICD^{nls} neurons. We therefore conclude that the Na^+ channels responsible for AP generation are not implicated in the AICD-dependent alteration of neuronal excitability.

To confirm our finding and exclude putative overexpression-related artifacts of virus-mediated *in vivo* expression, we used an alternative approach; i.e., we provided *ex vivo* intracellular delivery of AICD. We synthesized peptides representing AICD^{nls} or a negative scrambled control peptide (scrAICD^{nls}) linked at the N terminus to the cell-penetrating domain TAT (Guscott et al., 2016). We pre-incubated hippocampal slices with a dose of TAT-AICD^{nls} (100 nM), shown to induce an AICD intracellular increase in the range of values observed in an AD mouse model (Pousinha et al., 2017). Importantly, in this previous work, we confirmed that TAT-AICD^{nls} is enriched in the nucleus (Pousinha et al., 2017). Consistent to what we observed with 2 weeks *in vivo* expression of virally encoded AICD, *ex vivo* delivery of 100 nM TAT-AICD^{nls} reduced the firing frequency of CA1 pyramidal cells, an effect that was not observed with incubation of 100 nM control peptide (TAT-scrAICD^{nls}; Figure 1F). Furthermore, *ex vivo* delivery of AICD engages the same cellular mechanisms as *in vivo* virus-mediated AICD expression, as spike-frequency adaptation (Figure 1G) was increased in neurons from slices pre-incubated with TAT-AICD^{nls} (100 nM). Since the data obtained by using *in vivo* AICD intracellular increase pointed for a nuclear AICD-dependent mechanism, we examined the firing frequency properties of neurons from slices pre-incubated with TAT-AICD^{nls} or TAT-scrAICD^{nls} in presence of the inhibitor of gene transcription, actinomycin (25 μM). Actinomycin was added during both TAT peptides incubation and bath perfusion of slices. As shown (Figure 1H), TAT-AICD^{nls} failed to alter the neuronal firing frequency in the presence of this inhibitor, confirming a transcription-dependent effect.

AICD Decreases Neuron Firing through Enhancement of the Afterhyperpolarization

APs in hippocampal neurons are followed by a post-burst afterhyperpolarization potential (AHP) (Sah, 1996; Storm, 1990). The AHP is critical for the control of firing rate (Storm, 1990). Therefore, we hypothesized that AICD could alter neuronal intrinsic excitability through AHP enhancement. As AHP size is related to AP number during a sustained depolarization (Coulter et al., 1989), we examined the post-burst AHP elicited by a similar number of APs at a firing frequency shown to be impaired in AICD or AICD^{nls} neurons (12 APs at a frequency of 60 Hz; Figure 2A). We performed the post-burst AHP analysis by considering its medium (mAHP) (20–100 ms post-burst) and slow (sAHP) (400 ms to 4 s post-burst) components (Figure 2A), as both components have been described to affect CA1 neuron firing activity (Chen et al., 2014; King et al., 2015; Lancaster and Nicoll, 1987; Madison and Nicoll, 1984; Sah, 1996; Storm, 1990). As shown (Figures 2B and 2C), the mAHP was slightly enhanced in AICD neurons, becoming statistically significant in AICD^{nls} neurons, a modification not observed in AICD^{nes} neurons. Also, both sAHP full area and sAHP amplitude were enhanced in AICD^{nls} neurons (Figures 2D and 2E). A similar result was obtained upon analysis of post-burst AHP of CA1 pyramidal

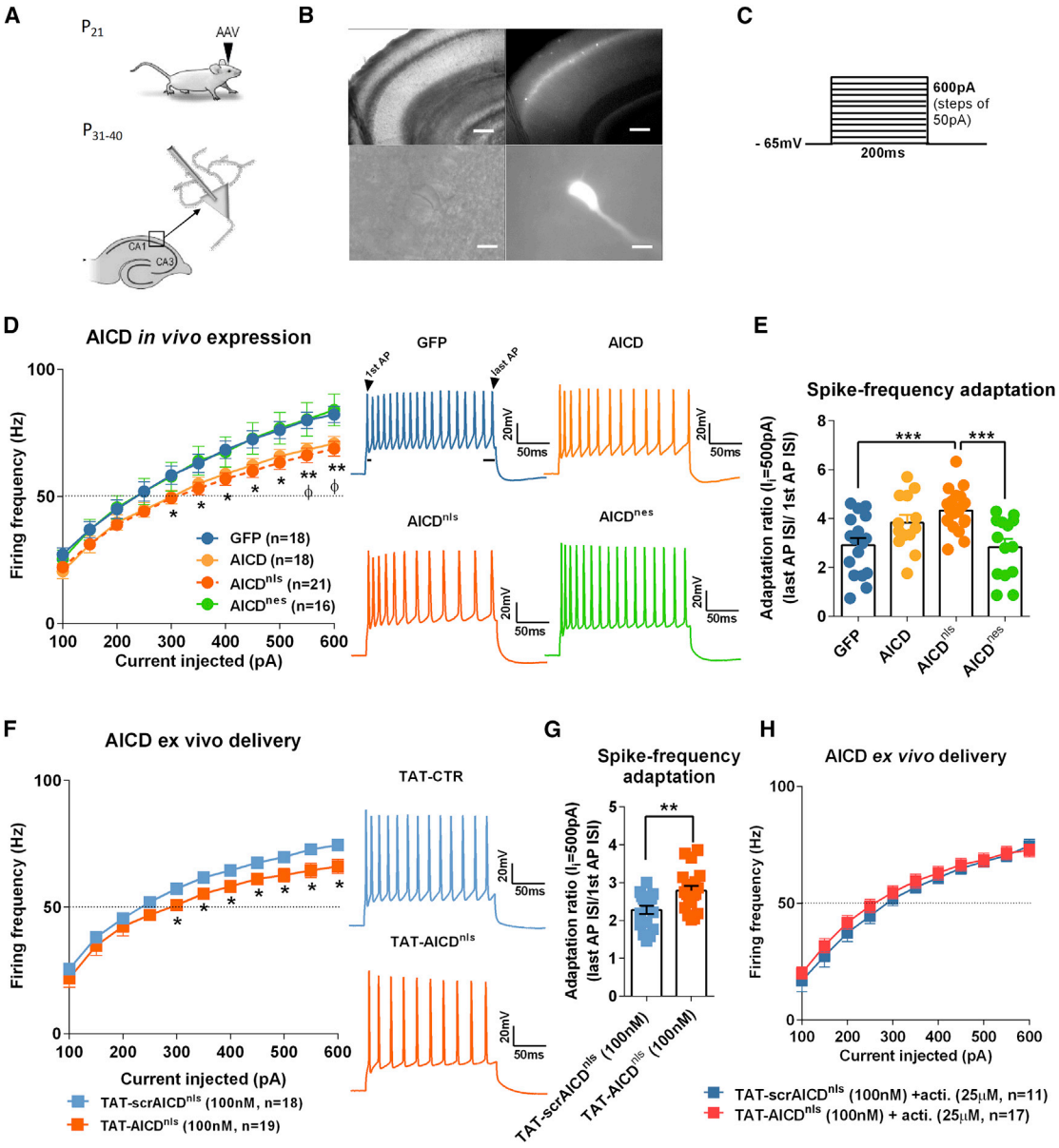

Figure 1. AICD Weakens CA1 Pyramidal Neuron Firing in the Gamma-Frequency Range through a Gene Transcription-Dependent Mechanism

(A) Diagram shows schematic of *in vivo* viral transduction protocol.

(B) Photos show low-magnification (×4; top panels; scale bars, 200 μm) and high-magnification (×60; bottom panels; scale bars, 10 μm) images of CA1 region of hippocampal slice (left panels show differential interference contrast [DIC] images; right panels show GFP fluorescence) prepared from rat transduced *in vivo* with $AICD^{nls}$.

(C) Protocol used for dissecting the supra-threshold CA1 pyramidal cells properties in the transduced neurons. 200-ms depolarizing current pulses, incrementing in steps of 50 pA, were applied at a pre-stimulus potential fixed at −65 mV.

(D, F, and H) Mean firing frequency versus injected current summary plot for (D) all tested virus (*$p < 0.05$, **$p < 0.01$ $AICD^{nls}$ compared to GFP and $AICD^{nes}$, $^{\phi}p < 0.05$ AICD compared to GFP and $AICD^{nes}$; two-way ANOVA with repeated measures); from slices pre-incubated in TAT-$scrAICD^{nls}$ or TAT-$AICD^{nls}$ peptides (100 nM) for 2 h, alone (F), or in the presence of the gene transcription inhibitor, actinomycin (acti., 25 μM) (H) (*$p < 0.05$, two-way ANOVA with repeated measures). On the right of (D) and (F), samples of AP trains in response to 500-pA current step.

(E and G) Scatter dot plot graphs of spike-frequency adaptation analysis based on the ratio concerning the interval inter stimulus (ISI) observed between the two last AP and between the two first AP from a train of APs triggered by 500-pA current step, observed on *in vivo* viral transduced neurons (E) and on neurons from slices pre-incubated in TAT-scrAICDnls or TAT-AICDnls peptides (100 nM) for 2 h (G).

Each dot in (E) and (G) represents one neuron, also indicated by n value in each panel (**$p < 0.01$ and ***$p < 0.001$, one-way ANOVA). Error bars represent the SEM. Statistic details are fully described in Table S1.

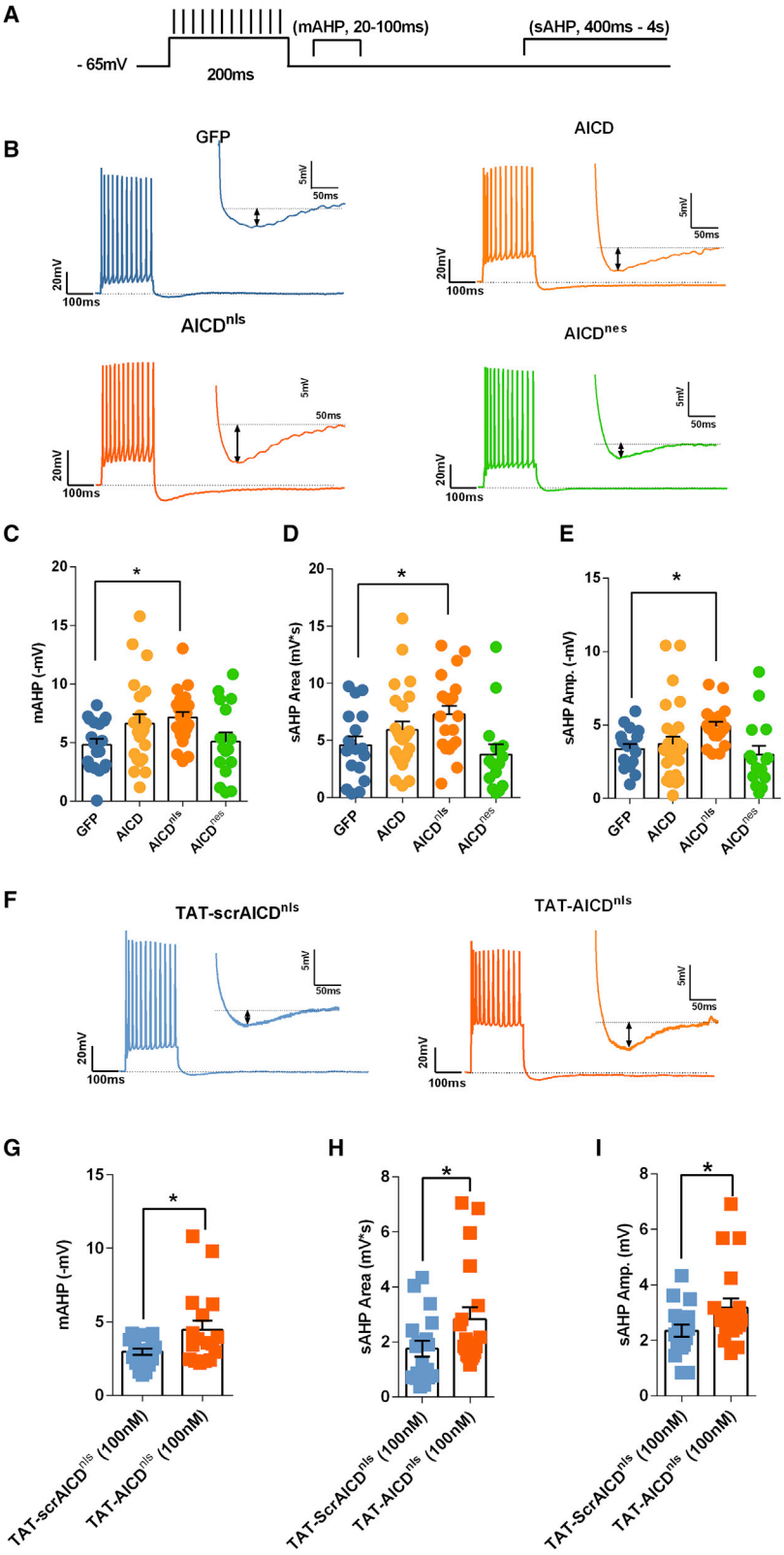

Figure 2. AICD Decreases Neuron Firing through Enhancement of the AHP

(A) Protocol used to trigger the AHP. Neurons were submitted to a depolarization current step sufficient to induce a train of 12 action potentials at 60 Hz.

(B and F) Examples of traces recorded from (B) transduced neurons or (F) neurons from slices pre-incubated in TAT-scrAICD^{nls} or TAT-AICD^{nls} peptides (100 nM) for 2 h, with insets where the AHP is presented on an expanded scale.

(C–E and G–I) Shown are scatter dot plot graphs of AICD-mediated effect on the mAHP amplitude (C and G), sAHP area (D and H), and sAHP amplitude (E and I) recorded in transduced neurons (C–E) or neurons from slices pre-incubated in TAT-scrAICD^{nls} or TAT-AICD^{nls} peptides (100 nM) for 2 h (G and H).

Each dot represents one neuron, also indicated by n value in each panel (*$p < 0.05$, one-way ANOVA or unpaired Student t test). Error bars represent the SEM. Statistic details are fully described in Table S2.

cells from slices pre-incubated in TAT-AICD^{nls} or TAT-scrAICD^{nls} peptides (Figures 2F–2I).

SK2 and KCa3.1 Channels Contribute to the AICD-Mediated Effect on CA1 Neuron Firing Activity

mAHP is highly sensitive to changes in intracellular Ca^{2+} (Lancaster and Zucker, 1994; Storm, 1987; Velumian and Carlen, 1999). In cortical neurons, the mAHP is mediated by small-conductance Ca^{2+}-activated K^+ channels (SK channels) (Villalobos et al., 2004), which are activated by intracellular Ca^{2+} ions, with submicromolar Ca^{2+} affinity (Köhler et al., 1996). In CA1 neurons, however, the mAHP is mediated by multiple ionic channels, where SK channels do not seem to be the main contributor (Chen et al., 2014; Gu et al., 2005). As AICD modulates the resting (Hamid et al., 2007) and evoked (Pousinha et al., 2017) intracellular calcium levels, we asked whether it could affect the charge transfer of SK channels, and therefore trigger an increased contribution of these channels to the mAHP. To test this hypothesis, we first investigated the effect of apamin, the SK channel-specific antagonist, on mAHP amplitude. As illustrated (Figure 3A), apamin failed to significantly alter the mAHP generation in GFP neurons. These data show that, physiologically, the mAHP in CA1 neurons is not mediated by SK channels, an observation that has previously been reported by others (Gu et al., 2005), who showed that in these neurons the mAHP is mediated by a complex of other ionic channels, including Kv7 channels. Interestingly, in the presence of apamin, all transduced neurons displayed an identical mAHP amplitude (Figure 3A). These data suggest that in the pathological context (increased AICDnls levels), the SK channel-mediated K^+ current significantly contributes to mAHP amplitude of CA1 excitatory neurons. In order to investigate whether the SK channel-mediated enhancement of the mAHP in AICDnls could affect neuron firing activity, we next performed the same protocol used to study supra-threshold CA1 pyramidal cells properties (200-ms depolarizing current pulses, incrementing in steps of 50 pA, applied at a pre-stimulus potential fixed at −65 mV; Figure 1A), but in the presence of apamin. We focused on AICD^{nls} neurons, which displayed the most significant increase in the mAHP amplitude. AP firing analysis showed that the AICD^{nls} firing frequency could be restored to control levels by apamin (100 nM) at all current injection steps (Figure 3B), strongly suggesting that SK channels charge transfer is increased in AICD^{nls} neurons. To corroborate this observation, we accessed the apamin-sensitive current (I_{SK}) of the I_{AHP}. To measure I_{AHP}, neurons were voltage clamped at −55 mV, and tail currents were evoked with a depolarizing step to +20 mV for 100 ms followed by a return to −55 mV (Figure 3C). The I_{SK} component was obtained by subtraction of the I_{AHP} measured before and after 30 min of apamin application. As shown (Figures 3D and 3E), in GFP neurons the apamin-sensitive component of the I_{AHP} was marginal. By contrast, the apamin-sensitive somatic current was significantly increased in AICD^{nls} neurons compared to GFP neurons (Figures 3D and 3E). Since SK channels are sensitive to intracellular calcium levels and we previously reported that AICD enhances N-methyl-D-aspartate receptor (NMDAR) conductance (Pousinha et al., 2017), we examined whether these receptors could be the source of Ca^{2+} leading to SK channels increased permeability. As shown, the NMDAR-selective antagonist (2*R*)-amino-5-phosphonovaleric acid (APV) (50 μM) failed to prevent the increase in I_{SK} observed in AICD^{nls} neurons (Figure 3E). Together, these data demonstrate that increased levels of AICD lead to over-activation of somatic SK channels, through an NMDAR-independent mechanism.

CA1 pyramidal neurons express the intermediate-conductance calcium-gated potassium channel KCa3.1, which contributes to the sAHP (King et al., 2015; Turner et al., 2016). Since AICD enhances both mAHP and sAHP, it is possible that AICD not only affects SK channels conductance, but also KCa3.1 channel function. Thus, we evaluated the sAHP amplitude and the firing excitability in neurons from slices pre-incubated in TAT-scrAICD^{nls} or TAT-AICD^{nls} in presence of the KCa3.1-selective inhibitor (TRAM-34). As shown (Figures 3F and 3G), the inhibition of KCa3.1 channels normalizes the sAHP amplitude and excitability profile of neurons from slices pre-incubated with TAT-AICD^{nls}, suggesting that these channels also contribute to the AICD-mediated effect on CA1 neuron firing activity.

The Effect of AICD on Neuron Firing Requires L-type Ca^{2+} Channels Activity

We next thought to identify the source of calcium that impacts SK- and KCa3.1-dependent postburst AHP increase in AICD neurons, as we previously excluded NMDAR (Figure 3E). We focused our attention on L-type voltage-dependent Ca^{2+} channels because these channels co-localize with SK and KCa3.1 channels in the somatodendritic compartment, with a spatial proximity that permits rapid regulation of these channels' conductance during APs (Marrion and Tavalin, 1998; Sahu et al., 2017). Accordingly, both L-type Ca^{2+} channel-selective blockers, nimodipine (5 μM) and isradipine (500 nM), could restore the firing frequency of neurons pre-incubated in TAT-AICD^{nls} to control (TAT-scrAICD^{nls}) values at all current injection steps (Figures 4A and S3A). To test whether AICD-related enhancement of AHP is due to enhanced L-type Ca^{2+} influx, we examined AHP components magnitude in presence of nimodipine or isradipine in neurons pre-incubated with either TAT-AICD^{nls} or TAT-scrAICD^{nls}. Blocking L-type Ca^{2+} channels with either drug prevented the effects of AICD on AHP (Figures 4B, 4C, S3B, and S3C). This indicates that increased AICD expression leads to an increase of L-type Ca^{2+} channels permeability, which stimulates Ca^{2+}-activated channels, namely SK and KCa3.1 channels, leading to enhanced AHP and, consequently, to hypoexcitability.

To directly test the influence of AICD on L-type calcium channels activity, we measured the nimodipine-sensitive current during a step current injection protocol (Figures 4D and 4E) in neurons pre-incubated with either TAT-AICD^{nls} or TAT-scrAICD^{nls}. L-type current magnitude was measured by subtraction of the selective inhibitor-resistant current from the total current after perfusion of the antagonist (Figure 4F), confirming that this current was enhanced by AICD^{nls}.

As SK, KCa3.1, and L-type calcium channel functions are all affected by AICD, and we show that these AICD modifications are transcription dependent, we investigated whether AICD could modify transcription of the genes encoding these channels. We treated rat hippocampal neuronal cultures (post-natal

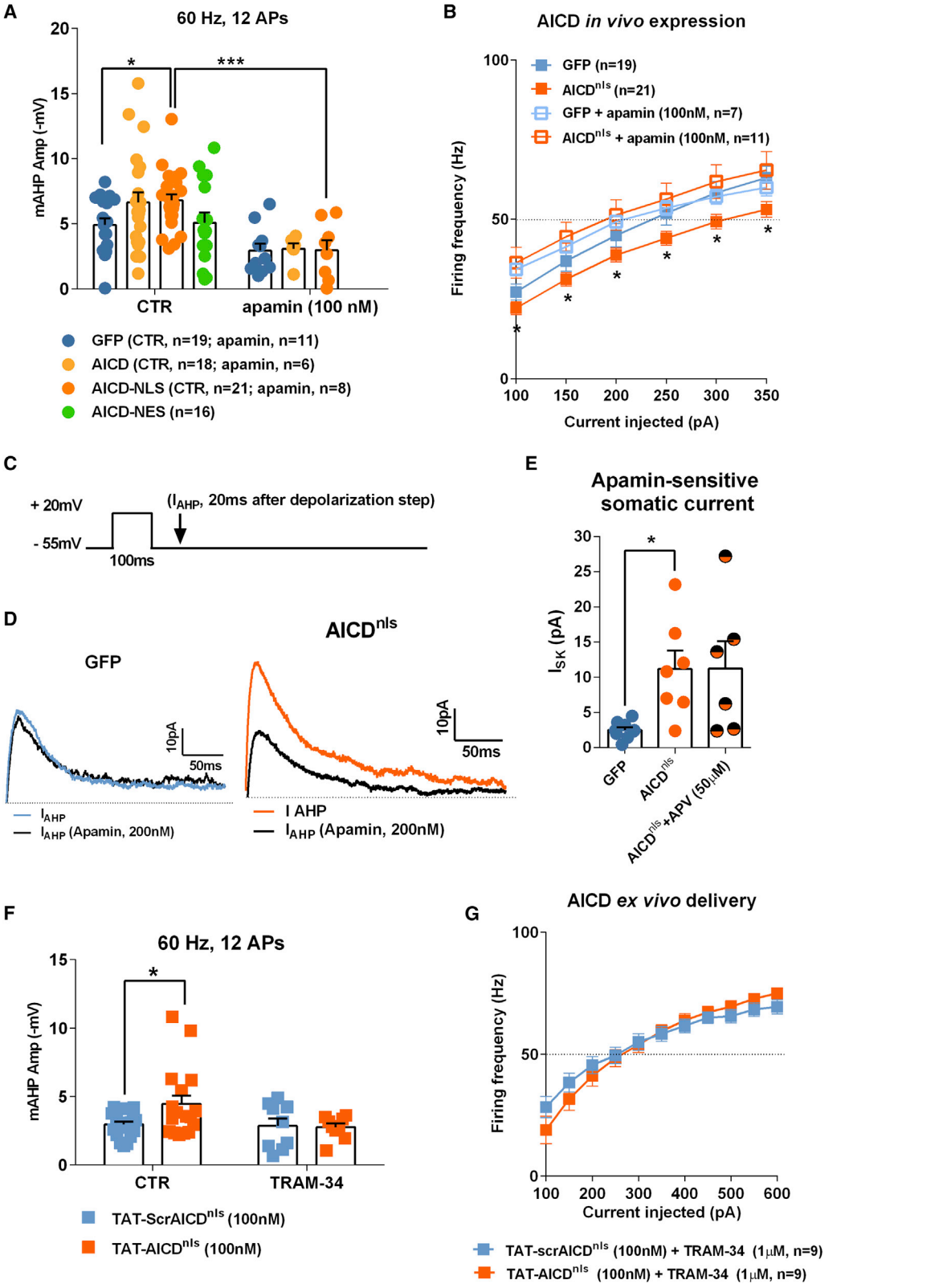

(legend on next page)

day 16 [P16] to P18) with TAT-scrAICDnls or TAT-AICDnls at a concentration of 100 nM for 2 h. We collected RNA and performed qPCR for quantification of SK2, KCa3.1, Cav1.2, and CaV1.3 genes. We did not observe any significant alterations in the transcription of these genes (Figures S3D–S3F), suggesting that AICD indirectly modulates their activity by promoting the transcription of other targets.

In Silico Experiments Predict that Increased AICD Production in CA1 Pyramidal Cells Impairs Hippocampus Gamma Oscillations

In order to further support and better explain the *ex vivo* experimental findings at the cellular level under somatic current injection, herein described and also recently reported (Pousinha et al., 2017), we performed *in silico* experiments. We used a CA1 pyramidal cell model previously validated against experimental findings and used to build a network model (Bianchi et al., 2014). Since this network model was originally based on mouse neuron properties, we first performed *ex vivo* whole-cell patch-clamp recordings in mouse neurons with increased *in vivo* AICD production to confirm that AICD effects on neuron excitability are species independent. As shown in Figure S4, the effect of AICD on mouse neuron firing activity is qualitatively similar to what we have described above in rat.

We optimized the neuron model to reproduce the number of spikes observed experimentally under control conditions as a function of a somatic current injection (Figures 5A and 5C). To reproduce the AICD effects, we found that a 50-fold increase of the sAHP current and a 60% increase in the L-calcium current was required in order to reduce the number of spikes as observed in the experiment. With these parameters, we were able to obtain a good replication of the experimental profile under the AICD condition (Figures 5B and 5D).

We next tested *in silico* what would happen in an individual CA1 pyramidal cell during an *in vivo* excitatory synaptic activity in the gamma range (a condition that would be extremely difficult to carry out experimentally). We carried out a set of simulations (n = 20) stimulating the neuron with synaptic inputs targeting the distal and proximal dendrites (to model excitatory EC and CA3 pathways, respectively). The results are shown in Figure 5E. Under control conditions (Figure 5E, left), the asynchronous activation of the synapses resulted in a tonic firing behavior at a relatively high frequency. After AICD, under exactly the same pattern of synaptic activation as in control (Figure 5E, right), the neurons displayed a much lower excitability, and the tonic firing behavior changed into a bursting activity. These effects were caused by the slow dynamics of the Ca^{2+}-dependent K^+ channels.

These results are in agreement with recently reported experimental findings (Pousinha et al., 2017) illustrating that AICD impairs synaptic signal integration when the neuron is stimulated at frequencies higher than 10 Hz. The power spectrum, obtained by averaging the somatic traces from 20 simulations (Figures 5F and 5G), showed that increased AICD production in these neurons can strongly reduce activity in the gamma range (40–80 Hz) without affecting theta oscillations (~4 Hz). Taken together, the model results suggest that the AICD-mediated decrease in CA1 pyramidal cell excitability can significantly impact hippocampus oscillations during synaptic activity.

In Vivo Production of AICD Elicits Spatial Memory Encoding Deficits

Hippocampal oscillatory activity has been described as a critical player in memory encoding, consolidation, and retrieval. We therefore asked whether animals with increased *in vivo* AICD production could present cognitive deficits. SynGFP or synAICD viruses (Figure S5) were injected bilaterally in dorsal hippocampi of 21-day-old male rats (Figure 6A). 15 days after *in vivo* virus transduction, the rats were subjected to a spatial object recognition task, which was recently demonstrated to require CA1 pyramidal cells gamma activity (Trimper et al., 2017; Zheng et al., 2016). Briefly, rats were first allowed to freely explore two identical objects for 5 min in a square arena (sample trial). After 20 min of rest, rats were replaced in the same arena and were allowed to explore the same objects presented before, but one of the two objects was displaced to a new location (test trial) (Figure 6B). Notably, synAICD rats showed a significant decrease in the preference for the object in a new location (Figures 6D and 6E). AICD-related alterations in locomotor or visual accuracy can be excluded as both groups (synGFP and synAICD) presented similar performances in the sample trial (Figure 6C), average speed (Figure 6F), and distance traveled (Figure 6G). Also, both groups presented similar thigmotaxis (Figure 6H) excluding a putative AICD effect on anxiety levels. These results clearly demonstrate that increased *in vivo* AICD production in neurons, in a restricted region of dorsal CA1 hippocampus of adult rats, is sufficient, per se, to impair spatial memory encoding.

Figure 3. SK2 and KCa3.1 Channels Contribute to the AICD-Mediated Effect on CA1 Neuron Firing Activity

(A) Scatter dot plot graphs showing that the selective SK channel blocker, apamin (100 nM), prevents AICD-mediated enhancement of mAHP amplitude.

(B) Mean firing frequency versus injected current summary plot for neurons transduced with GFP and $AICD^{nls}$ viruses in absence or presence of apamin (100 nM).

(C) Protocol used to measure the I_{AHP}. Neurons were voltage clamped at −55 mV, and tail currents were evoked with a depolarizing step to +20 mV for 100 ms followed by a return to −55 mV.

(D) Representative traces of the I_{AHP}, seen as an outward tail current, from GFP and $AICD^{nls}$ transduced neurons before (black trace) and after (gray trace) bath application of apamin (100 nM).

(E) Scatter dot plot graph show the subtracted apamin-sensitive current, I_{SK} amplitude (I_{AHP} before apamin perfusion – I_{AHP} after apamin perfusion) observed in GFP and $AICD^{nls}$ transduced neurons. The NMDAR selective blocker, APV (50 μM) failed to prevent $AICD^{nls}$ effect.

(F and G) Scatter dot plot graph of the sAHP amplitude (F) and mean firing frequency versus injected current summary plot (G) in control condition or presence of the selective KCA3.1 channel blocker, TRAM-34 (1 μM) for neurons from slices pre-incubated in TAT-$scrAICD^{nls}$ or TAT-$AICD^{nls}$ peptides (100 nM) for 2 h.

Each dot in (A) and (E) and (F) represents one neuron, also indicated by n value in each panel (***$p < 0.0001$, two-way-ANOVA; *$p < 0.05$, two-way or one-way ANOVA). Error bars represent the SEM.

Statistic details are fully described in Table S3.

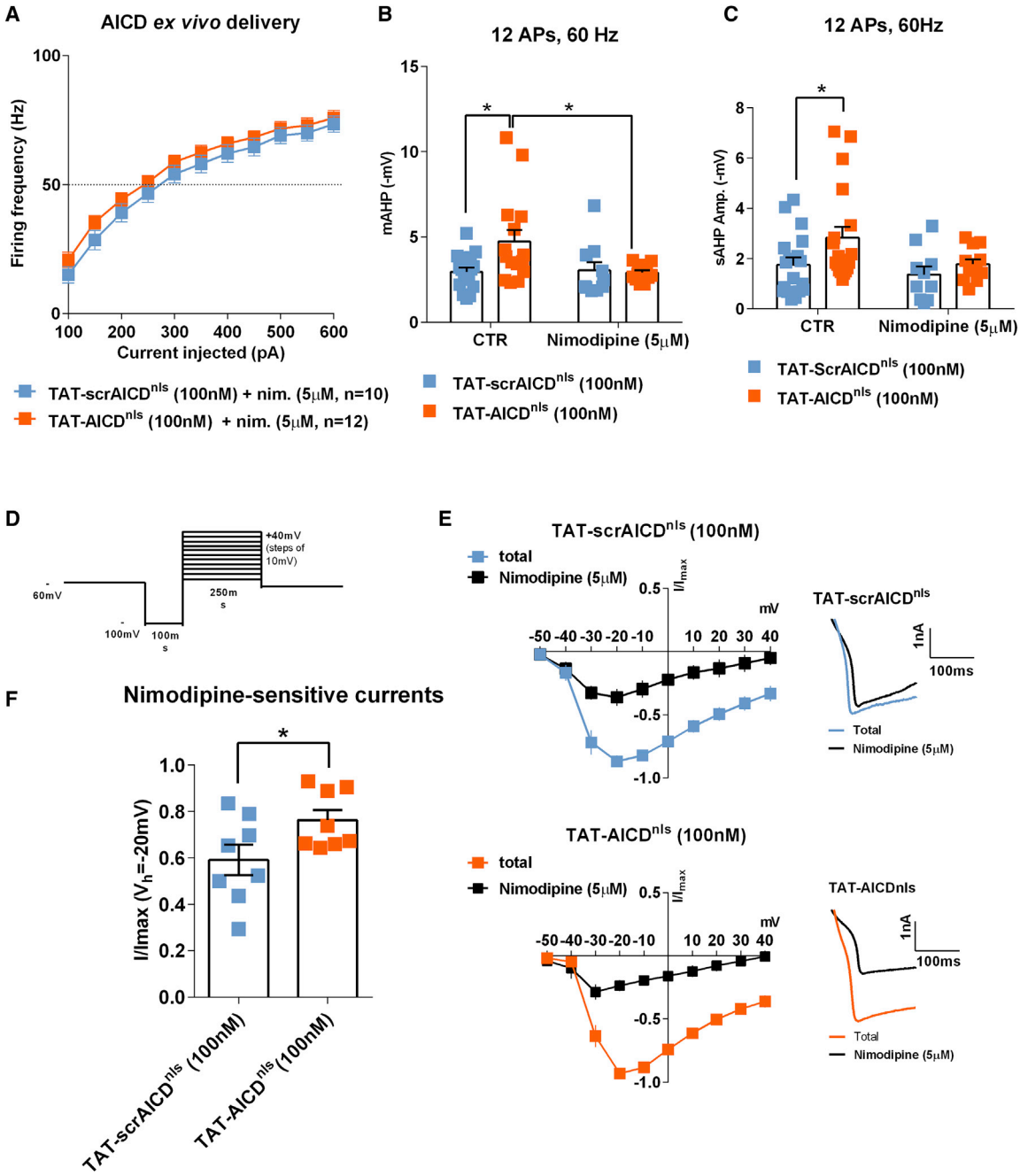

Figure 4. The Effect of AICD on Neuron Firing Requires L-type Ca^{2+} Channel Activity

(A) Mean firing frequency versus injected current summary plot recorded in neurons from slices pre-incubated in TAT-scrAICD^{nls} or TAT-AICD^{nls} peptides (100 nM) for 2 h, and after recorded in the presence of the L-type Ca^{2+} channels blocker, nimodipine (5 μM), in the bath perfusion (nim., nimodipine).

(B and C) Scatter dot plot graphs showing (B) mAHP and (C) sAHP amplitude (Vm-V_h, where V_h = −65 mV) recorded from neurons submitted to a depolarization current step sufficient to induce a train of 12 APs at 60 Hz.

(D) Protocol used to measure the nimodipine-sensitive current. Neurons were voltage clamped at −60 mV, and tail currents were evoked with a hyperpolarizing step to −100 mV for 100 ms followed by 200-ms depolarizing current pulses, incrementing in steps of 10 pA and return to −60 mV.

(E) I-V plot of whole-cell calcium currents before and after nimodipine (5 μm) application, where I/I_{max} is the current normalized to the maximal current of each cell. On the right representative traces of whole-cell calcium current elicited by a voltage step from −100 to +10 mV, before and after nimodipine (5 μm) application.

(F) Scatter dot plot graph shows the subtracted nimodipine-sensitive current in the recorded neurons (*p < 0.05, two-way ANOVA or unpaired Student t test). Each dot in (B), (C), and (F) represents one neuron, also indicated by n value in each panel. Error bars represent the SEM.

Statistic details are fully described in Table S4.

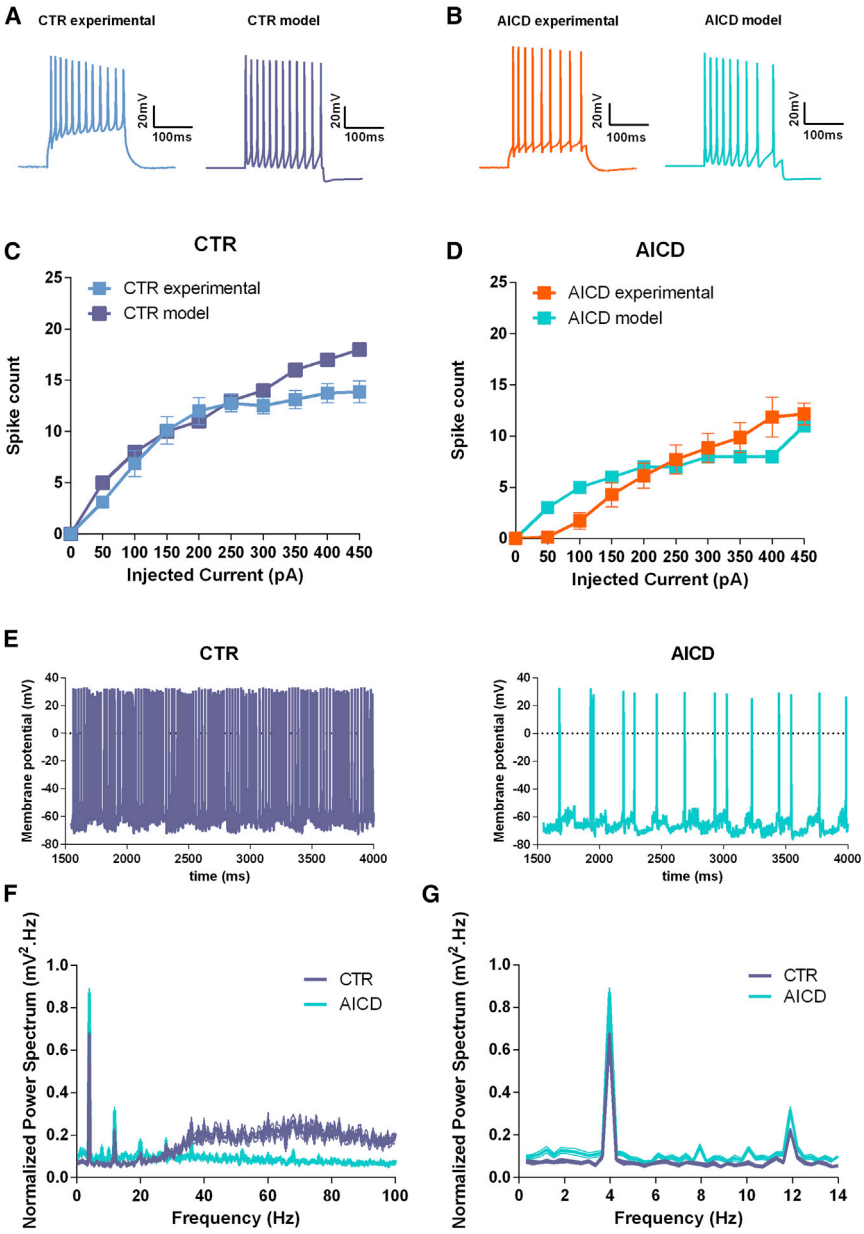

Figure 5. Computational Model of AICD Effects

(A and B) Typical traces from somatic current injections in control (A) and AICD (B) neurons for I = 0.3 nA under experimental and *in silico* model situations.

(C and D) Number of spikes elicited as a function of the somatic current injection under control (C) or AICD (D).

(E) Typical traces from *in silico* synaptic simulations under control (Ctrl) (left) and AICD (right) conditions.

(F and G) Normalized power spectrum calculated from 20 simulations under control or AICD conditions for frequencies of 0–150 Hz (F) and same graph zoomed in for frequencies of 0–15 Hz (G); lines represent the average and the SEM.

Statistic details are fully described in Table S5.

DISCUSSION

Here, we provide strong evidence that AICD, at pathological levels, is a critical trigger for disruption of CA1 neuron firing activity, alteration of hippocampal network oscillations, and impairment in spatial memory encoding. Notably, we could unravel the cellular mechanism underlying AICD-mediated hypoexcitability of CA1 pyramidal cells. Briefly, when a neuron with increased AICD levels receives inputs to fire at high frequency, an alteration in the L-type Ca^{2+} channels causes an increased Ca^{2+}-sensitive AHP, weakening its firing frequency. We showed evidence that this effect is mediated by Ca^{2+}-activated K^+ channels, namely SK and KCa3.1 channels. Also, *in silico* experiments revealed an AICD-mediated alteration of hippocampal network oscillations, specifically affecting gamma rhythms. In agreement, animals with increased AICD levels in the dorsal hippocampus failed to recognize a familiar object in a novel location, a task that was recently reported to recruit CA1 pyramidal neurons firing at gamma frequency (Trimper et al., 2017; Zheng et al., 2016).

We gathered solid data advocating that AICD exerts its effect on neuron firing activity through a transcription-dependent mechanism. Besides the fact that AICD and $AICD^{nls}$ displayed a similar phenotype, albeit sometimes more pronounced in $AICD^{nls}$ neurons, we could prevent these effects in the presence of a gene transcription inhibitor, actinomycin, or by expelling AICD from the nucleus ($AICD^{nes}$). Accordingly, AICD is a transcription factor able to modulate transcription of a number of genes (Beckett et al., 2012; Bukhari et al., 2017; Grimm et al., 2013; Konietzko, 2012; Pardossi-Piquard and Checler, 2012) through interaction with cofactors/nuclear modulators (Bukhari et al., 2017; Cupers et al., 2001; Grimm et al., 2013; Kimberly et al., 2001).

In agreement with our results, several studies demonstrate that blocking L-type Ca^{2+} channels leads to a reduction of the postburst AHP in hippocampal neurons (Kumar and Foster, 2002), and Santos et al. (2009) reported that expression of full-length human APP in rat cortical neuron cultures enhances the AHP, inhibiting calcium oscillations, through a similar mechanism (L-type Ca^{2+} channels–Ca^{2+}-activated K^+ channels coupling), that we herein describe. In the past few years, several authors reported that in CA1 hippocampal neurons, SK channels play an auxiliary role in controlling the intrinsic excitability of these neurons (Gu et al., 2005; Chen et al., 2014), barely contributing to the generation of the mAHP in physiological conditions,

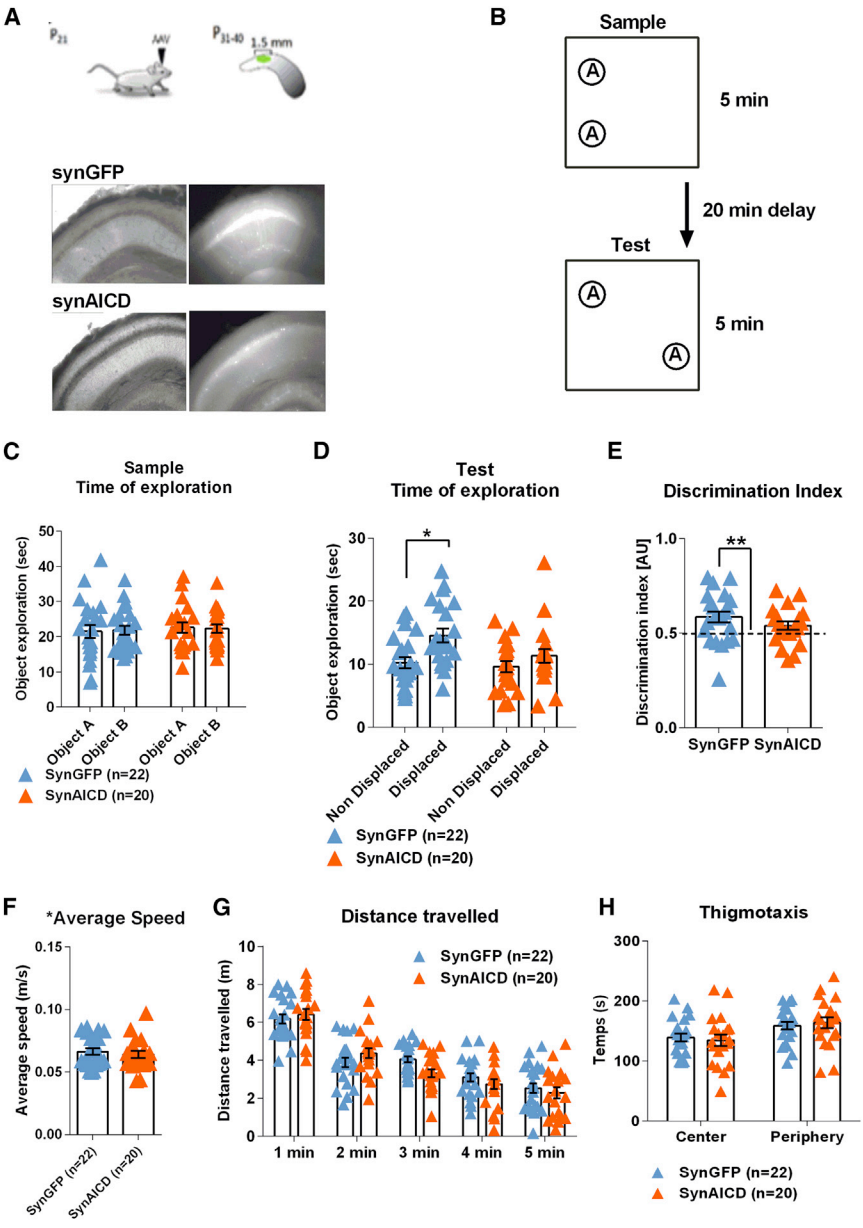

Figure 6. *In Vivo* Production of AICD Elicits Spatial Memory Encoding Deficits

(A) Top: diagram shows schematic of *in vivo* viral transduction protocol with AVV injections at P21 and post-behavioral hippocampal transduction spreading analysis at P40. Bottom: photos show low-magnification (×4) images of CA1 area of hippocampal slice (left panels show IR-DIC images; right panels show GFP fluorescence) prepared from rat injected *in vivo* with synGFP or synAICD, as indicated.

(B) Diagram illustrating behavioral task to test hippocampus-dependent spatial memory encoding, adapted from Zheng et al. (2016), in synGFP and synAICD rats.

(C and D) Scatter dot plot graphs representing: (C) total object exploration during sample trial and (D) time of exploration during the test trial, where one of the objects is presented in a new location (displaced) (*p < 0.05, two-way ANOVA).

(E) Discrimination index (**p < 0.01, one-sample Student's t test).

(F) Average speed during the test trial.

(G) Distance traveled per bins of 1 min during test trial.

(H) Thigmotaxis during test trial. The blue triangles (synGFP) and orange triangles (synAICD) correspond to animals (22 and 20, respectively).

Error bars represent the SEM.

Statistic details are fully described in Table S6.

as we could also observe in GFP neurons. Chen and colleagues (2014) showed that when the activity of the main contributors to the mAHP in CA1 neurons, the low-voltage Kv7/M channels, is compromised, SK channels take charge of reducing spike output of these neurons. Since our data and the work of Santos et al. (2009) show a significant contribution of SK channels to the mAHP in CA1 pyramidal cells, it is plausible to consider that in pathological conditions the molecular mechanisms underlying the mAHP generation change. As corollary to enhanced SK contribution in these conditions, an additional decrease of the low-voltage Kv7/M channels contribution can thus not be excluded. Of note, Santos et al. (2009) did not address a putative APP gene-transcription-dependent mechanism. These results suggest that increased expression of the full-length APP protein or its C-terminal fragment AICD can trigger similar signaling cascade of events to modulate neuronal firing homeostasis. Indeed, the full-length APP-mediated inhibitory effect on calcium oscillations was shown to be dependent on APP-T668 phosphorylation (Santos et al., 2011), a residue located in the intracellular domain crucial for the binding of APP to other intracellular proteins such as Fe65 or Pin1 (Ando et al., 2001; Pastorino et al., 2006) and known to be implicated in AICD-nuclear signaling (Goodger et al., 2009; Grimm et al., 2015; Kimberly et al., 2001).

Conspicuously, an imbalance in AICD levels, and therefore function, seems to cause detrimental cellular impact by modifying calcium permeability at both synapse and soma. In another recent study (Pousinha et al., 2017), we demonstrated that, at synapses, APP deletion leads to the loss of synaptic GluN2B-NMDARs, a phenotype rescued by AICD delivery; whereas increasing AICD levels enhances synaptic GluN2B-NMDARs currents. Accordingly, N2a cells with suppressed levels of AICD present reduced endoplasmic reticulum (ER) Ca^{2+} storage (Hamid et al., 2007), while cells with enhanced levels of AICD show increased ER Ca^{2+} filling (Leissring et al., 2002). Intracellular Ca^{2+} homeostasis greatly relies on the rapid redistribution of Ca^{2+} ions into the diverse subcellular organelles, which serve as Ca^{2+} stores, including the ER (Brini and Carafoli, 2009;

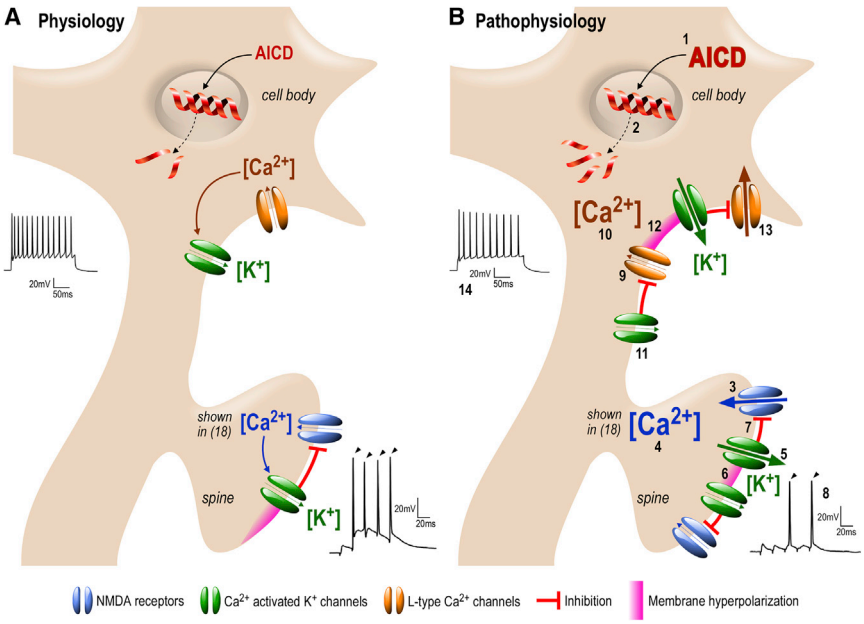

Figure 7. Emerging Model for AICD Pathological Effects on Neuronal Function

(A and B) Here, we show two comparative panels illustrating two scenarios: physiology (A) and pathology due to increased levels of AICD (B). As indicated in (B), when AICD levels are increased to pathological levels, it acts both at the spines (3 to 8) and at the soma (9 to 14), changing the sensitivity of the neuron to the inputs. AICD translocates to the nucleus (1), where it modulates gene transcription (2) through yet-unknown mechanisms. At the synapse (as reported in Pousinha et al., 2017), increased AICD leads to NMDAR conductance upregulation (3), leading to increased Ca^{2+} permeability (4), which in turn activates the nearby Ca^{2+} activated K^+ channels (5). These channels are K^+ permeable, causing a hyperpolarization of the cell membrane (6), hence inhibiting NMDA receptors (7) and, consequently, perturbing synaptic signal integration (8). At the soma, pathological levels of AICD trigger increased Ca^{2+} permeability through L-type Ca^{2+} channels (9, 10), thus leading to close-by Ca^{2+}-activated K^+ channels opening (11). As K^+ exits the cell, the membrane becomes hyperpolarized (12), producing an increased Ca^{2+}-sensitive AHP (13), thus decreasing neuron firing activity (14). Together, these mechanisms contribute to neuron firing homeostasis failure, in particular at high frequencies, thus impairing the signal output and therefore the associated memory processes. The increase in ionic channel numbers in the physiopathological condition is for graphical purposes only as we do not at present hold evidence for any AICD-induced increase in cell surface expression of these channels.

Burdakov et al., 2005; Clapham, 1995; Wuytack et al., 2002). Notably, AICD effects on calcium homeostasis were not observed when cells were incubated in Ca^{2+}-free medium (Hamid et al., 2007). Together, these previous data and our current study strongly suggest that AICD effects on Ca^{2+} homeostasis are due to alterations in plasma membrane calcium permeability, likely involving NMDARs and L-type Ca^{2+} channels.

Of note, we observed common features in the cellular mechanisms underlying the action of AICD in our other recent study, focused at the synapse (Pousinha et al., 2017), and in the present work, focused at the cell body. In both studies, the physiopathological actions of AICD are gene-transcription-dependent and independent of *in vivo* chronic expression. Moreover, in both studies, calcium channels present at the plasma membrane are affected by AICD in a frequency-dependent manner. However, AICD alters NMDAR to modulate synapse function, whereas it modulates L-type Ca^{2+} channels to modify firing homeostasis. In both situations, AICD leads to increased calcium entry, hence rendering the membrane hyperpolarized via Ca^{2+}-activated K^+ channels overactivation. Thus, AICD specifically affects calcium channels that are functionally coupled to Ca^{2+} activated K^+ channels in distinct spatial regions of the neuron: spine and cell body (Köhler et al., 1996; Marrion and Tavalin, 1998). Overall, it is plausible to advocate that AICD synaptic and somatic effects perturb neuron homeostatic machinery, tuning down the sensitivity of CA1 excitatory neurons to the incoming inputs, reducing its chance to participate in a given memory trace.

The mean firing rate, reflecting an average level of spontaneous spiking activity, is under homeostatic control in central neural circuits, as recently demonstrated in both *ex vivo* (Slomowitz et al., 2015) and *in vivo* (Hengen et al., 2016) models. Thus, homeostatic mechanisms stabilize neural circuit function by keeping firing rates within a set-point range, by, for example, adjusting the Ca^{2+}-sensitive AHP, which is critical for the control of neuron firing activity (Storm, 1990). All transmembrane currents contribute to brain rhythms, in particular Na^+ currents that are generated by APs (Buzsáki et al., 2012). We could show, through *in silico* modeling, that increased AICD production in CA1 pyramidal cells can strongly reduce their activity within the gamma-rhythm range (40–80 Hz) without affecting theta oscillations (~4 Hz). These results are in agreement with our original hypothesis: that increased levels of AICD cause CA1 pyramidal cells hypoactivity specifically at inputs of high frequency. Gamma oscillations have been attributed to various cognitive processes including hippocampus memory encoding (Lisman and Idiart, 1995; Zheng et al., 2016). Notably, we now show that increased AICD production in a restricted area of dorsal hippocampus is sufficient to impair object recognition in a novel location, a task recently attributed to CA1 place cell firing at gamma frequency (Zheng et al., 2016), thus suggesting a causality between AICD-associated CA1 pyramidal cells decreased firing and hippocampal cognitive deficits.

Both physiological aging and AD comprehend functional and structural alterations in the hippocampus that drive cognitive decline. Therefore, it is conceivable to hypothesize that the shift from normal aging to AD could be related to common pathophysiological events, which become exacerbated in the neurodegenerative disorder. Intriguingly, our results highly correlate with observations reported in CA1 neurons from aged rodents. One of the well-characterized markers of physiological aging is an age-related decrease in AP firing rates of CA1 pyramidal cells,

with a concomitant increase in the amplitude of the AHP responsible for spike frequency adaptation (Disterhoft et al., 1996; Landfield and Pitler, 1984; Power et al., 2002). Moreover, although the molecular mechanisms responsible for these alterations in aging brains are still not fully understood, several studies suggest that it is due to L-type calcium channels dysregulation. Indeed, their charge transfer is enhanced in aged hippocampal neurons (Núñez-Santana et al., 2014; Veng et al., 2003), and their antagonists can counteract the effects of aging on cognition (Rose et al., 2007; Veng et al., 2003). A provocative interpretation may arise from these similarities: AICD age-related progressive upregulation, likely due to either a lower degradation rate linked to reduced expression of its insulin-degrading enzyme (Cook et al., 2003; Nalivaeva and Turner, 2017) or increased production triggered by BACE1 enhanced expression (Ahmed et al., 2010; Holsinger et al., 2002), may contribute to the shift from physiological aging to AD.

Our observations extend the knowledge on AICD pathological role strengthening its contribution to AD pathogenesis. Although more work is needed to understand precisely the nuclear AICD targets/mechanisms that modify membrane calcium channel permeability, we propose an emerging model based on our recent work (Pousinha et al., 2017) and the results herein described (Figure 7). Increased AICD levels lead to enhanced membrane calcium permeability through synaptic GluN2B-NMDAR and somatic L-type Ca^{2+} channels, which activate the nearby Ca^{2+}-activated K^+ channels, rendering the neuron hypoactive. Thus, AICD decreases neuron sensitivity to excitatory synaptic inputs and, simultaneously, reduces its ability to fire at gamma frequency when solicited. Together, these AICD-triggered modifications will impede normal neuron responses to experience-driven stimuli, hence impairing the underlying memory tasks, like spatial memory encoding. More broadly, the current findings highlight common features between physiological aging and AD, thus suggesting that AICD might correlate with progressive neuron homeostatic failure, driving the transition from synaptic and cognitive impairments, observed in physiological aging, to neurodegeneration.

STAR★METHODS

Detailed methods are provided in the online version of this paper and include the following:

- KEY RESOURCES TABLE
- LEAD CONTACT AND MATERIALS AVAILABILITY
- EXPERIMENTAL MODEL AND SUBJECT DETAILS
  - Animals
  - Primary neuronal cultures
- METHOD DETAILS
  - Virus Constructs
  - TAT peptides
  - *In Vivo* AAV Injections
  - Quantitative PCR in primary neuronal cultures
  - Pharmacological tools
  - Patch-Clamp Electrophysiology
  - *In silico* modeling
  - Behavioral analysis
- QUANTIFICATION AND STATISTICAL ANALYSES
- DATA AND CODE AVAILABILITY

SUPPLEMENTAL INFORMATION

Supplemental Information can be found online at https://doi.org/10.1016/j.celrep.2019.08.103.

ACKNOWLEDGMENTS

This work was supported by the ATIP/AVENIR program (Centre National de la Recherche Scientifique [CNRS]) to P.A.P. and H.M.; Fondation pour la Recherche Médicale (FRM; postdoctoral fellowship) to P.A.P.; the French Fondation Plan Alzheimer to E.F.R., X.M., and H.M.; the EU Joint Program–Neurodegenerative Disease Research (JPND) Project CIRCPROT (jointly funded by BMBF, MIUR, and EU Horizon 2020 Grant Agreement 643417) to H.M. and P.A.P., D.B., and M.M.; EU Horizon 2020 Framework Programme for Research and Innovation (Specific Grant Agreement 785907; Human Brain Project SGA2); the Université Côte d'Azur to H.M. and P.A.P.; Santa Casa da Misericórdia (MB-7-2018); and Fundação para a Ciência e Tecnologia (PD/BD/135516/2018, SFRH/BD/52228/2013, and PTDC/BIMMEC/4778/2014) to L.V.L., J.R.-S., and M.T.-F. We thank Maxime Villet for behavioral data analysis and Frank Aguila for the design of illustrations presented in Figure 7 and the Graphical Abstract.

AUTHOR CONTRIBUTIONS

P.A.P. and H.M. designed the study and interpreted the results. P.A.P. performed *ex vivo* electrophysiological recordings and analysis and helped with behavioral assays. P.A.P. and S.P.F. performed *in vivo* stereotaxic surgeries. E.F.R., X.M., and H.M. produced viruses, cloned viruses, and performed biochemical analysis. R.G. designed the primers. M.T.-F., J.R.-S., and L.V.L. prepared and performed the qPCR on hippocampal neuron cultures. I.B. and A.R.S.-P. performed behavioral assays. C.G. performed histology. R.G. and J.B. provided intellectual and technical inputs. D.B. and M.M. designed and performed all of the modeling. P.A.P. wrote the manuscript with input from the other authors.

DECLARATION OF INTERESTS

The authors declare no conflict of interest.

Received: August 10, 2018
Revised: August 9, 2019
Accepted: August 29, 2019
Published: October 8, 2019

REFERENCES

Ahmed, R.R., Holler, C.J., Webb, R.L., Li, F., Beckett, T.L., and Murphy, M.P. (2010). BACE1 and BACE2 enzymatic activities in Alzheimer's disease. J. Neurochem. *112*, 1045–1053.

Ando, K., Iijima, K.I., Elliott, J.I., Kirino, Y., and Suzuki, T. (2001). Phosphorylation-dependent regulation of the interaction of amyloid precursor protein with Fe65 affects the production of beta-amyloid. J. Biol. Chem. *276*, 40353–40361.

Bean, B.P. (2007). The action potential in mammalian central neurons. Nat. Rev. Neurosci. *8*, 451–465.

Beckett, C., Nalivaeva, N.N., Belyaev, N.D., and Turner, A.J. (2012). Nuclear signalling by membrane protein intracellular domains: the AICD enigma. Cell. Signal. *24*, 402–409.

Benda, J., Longtin, A., and Maler, L. (2005). Spike-frequency adaptation separates transient communication signals from background oscillations. J. Neurosci. *25*, 2312–2321.

Bianchi, D., De Michele, P., Marchetti, C., Tirozzi, B., Cuomo, S., Marie, H., and Migliore, M. (2014). Effects of increasing CREB-dependent transcription on the storage and recall processes in a hippocampal CA1 microcircuit. Hippocampus *24*, 165–177.

Brini, M., and Carafoli, E. (2009). Calcium pumps in health and disease. Physiol. Rev. *89*, 1341–1378.

Brown, J.T., Chin, J., Leiser, S.C., Pangalos, M.N., and Randall, A.D. (2011). Altered intrinsic neuronal excitability and reduced Na^+ currents in a mouse model of Alzheimer's disease. Neurobiol. Aging *32*, 2109.e1–2109.e14.

Bukhari, H., Glotzbach, A., Kolbe, K., Leonhardt, G., Loosse, C., and Müller, T. (2017). Small things matter: implications of APP intracellular domain AICD nuclear signaling in the progression and pathogenesis of Alzheimer's disease. Prog. Neurobiol. *156*, 189–213.

Burdakov, D., Petersen, O.H., and Verkhratsky, A. (2005). Intraluminal calcium as a primary regulator of endoplasmic reticulum function. Cell Calcium *38*, 303–310.

Bustin, S.A., Benes, V., Garson, J.A., Hellemans, J., Huggett, J., Kubista, M., Mueller, R., Nolan, T., Pfaffl, M.W., Shipley, G.L., et al. (2009). The MIQE guidelines: minimum information for publication of quantitative real-time PCR experiments. Clin. Chem. *55*, 611–622.

Buzsáki, G., Anastassiou, C.A., and Koch, C. (2012). The origin of extracellular fields and currents—EEG, ECoG, LFP and spikes. Nat. Rev. Neurosci. *13*, 407–420.

Chen, S., Benninger, F., and Yaari, Y. (2014). Role of small conductance Ca^{2+}-activated K^+ channels in controlling CA1 pyramidal cell excitability. J. Neurosci. *34*, 8219–8230.

Clapham, D.E. (1995). Intracellular calcium. Replenishing the stores. Nature *375*, 634–635.

Colbert, C.M., Magee, J.C., Hoffman, D.A., and Johnston, D. (1997). Slow recovery from inactivation of Na+ channels underlies the activity-dependent attenuation of dendritic action potentials in hippocampal CA1 pyramidal neurons. J. Neurosci. *17*, 6512–6521.

Cook, D.G., Leverenz, J.B., McMillan, P.J., Kulstad, J.J., Ericksen, S., Roth, R.A., Schellenberg, G.D., Jin, L.-W., Kovacina, K.S., and Craft, S. (2003). Reduced hippocampal insulin-degrading enzyme in late-onset Alzheimer's disease is associated with the apolipoprotein E-epsilon4 allele. Am. J. Pathol. *162*, 313–319.

Coulter, D.A., Lo Turco, J.J., Kubota, M., Disterhoft, J.F., Moore, J.W., and Alkon, D.L. (1989). Classical conditioning reduces amplitude and duration of calcium-dependent afterhyperpolarization in rabbit hippocampal pyramidal cells. J. Neurophysiol. *61*, 971–981.

Cupers, P., Orlans, I., Craessaerts, K., Annaert, W., and De Strooper, B. (2001). The amyloid precursor protein (APP)-cytoplasmic fragment generated by gamma-secretase is rapidly degraded but distributes partially in a nuclear fraction of neurones in culture. J. Neurochem. *78*, 1168–1178.

De Strooper, B., and Karran, E. (2016). The cellular phase of Alzheimer's disease. Cell *164*, 603–615.

Disterhoft, J.F., Thompson, L.T., Moyer, J.R., Jr., and Mogul, D.J. (1996). Calcium-dependent afterhyperpolarization and learning in young and aging hippocampus. Life Sci. *59*, 413–420.

Frere, S., and Slutsky, I. (2018). Alzheimer's disease: from firing instability to homeostasis network collapse. Neuron *97*, 32–58.

Ghosal, K., Vogt, D.L., Liang, M., Shen, Y., Lamb, B.T., and Pimplikar, S.W. (2009). Alzheimer's disease-like pathological features in transgenic mice expressing the APP intracellular domain. Proc. Natl. Acad. Sci. USA *106*, 18367–18372.

Gillespie, A.K., Jones, E.A., Lin, Y.-H., Karlsson, M.P., Kay, K., Yoon, S.Y., Tong, L.M., Nova, P., Carr, J.S., Frank, L.M., and Huang, Y. (2016). Apolipoprotein E4 causes age-dependent disruption of slow gamma oscillations during hippocampal sharp-wave ripples. Neuron *90*, 740–751.

Goodger, Z.V., Rajendran, L., Trutzel, A., Kohli, B.M., Nitsch, R.M., and Konietzko, U. (2009). Nuclear signaling by the APP intracellular domain occurs predominantly through the amyloidogenic processing pathway. J. Cell Sci. *122*, 3703–3714.

Grimm, M.O., Mett, J., Stahlmann, C.P., Haupenthal, V.J., Zimmer, V.C., and Hartmann, T. (2013). Neprilysin and Aβ clearance: impact of the app intracellular domain in NEP regulation and implications in Alzheimer's disease. Front. Aging Neurosci. *5*, 98.

Grimm, M.O., Mett, J., Stahlmann, C.P., Grösgen, S., Haupenthal, V.J., Blümel, T., Hundsdörfer, B., Zimmer, V.C., Mylonas, N.T., Tanila, H., et al. (2015). APP intracellular domain derived from amyloidogenic β- and γ-secretase cleavage regulates neprilysin expression. Front. Aging Neurosci. *7*, 77.

Gu, N., Vervaeke, K., Hu, H., and Storm, J.F. (2005). Kv7/KCNQ/M and HCN/h, but not KCa2/SK channels, contribute to the somatic medium after-hyperpolarization and excitability control in CA1 hippocampal pyramidal cells. J. Physiol. *566*, 689–715.

Guscott, B., Balklava, Z., Safrany, S.T., and Wassmer, T. (2016). A cell-permeable tool for analysing APP intracellular domain function and manipulation of PIKfyve activity. Biosci. Rep. *15*, e00319.

Hamid, R., Kilger, E., Willem, M., Vassallo, N., Kostka, M., Bornhövd, C., Reichert, A.S., Kretzschmar, H.A., Haass, C., and Herms, J. (2007). Amyloid precursor protein intracellular domain modulates cellular calcium homeostasis and ATP content. J. Neurochem. *102*, 1264–1275.

Hammond, R.S., Bond, C.T., Strassmaier, T., Ngo-Anh, T.J., Adelman, J.P., Maylie, J., and Stackman, R.W. (2006). Small-conductance Ca^{2+}-activated K^+ channel type 2 (SK2) modulates hippocampal learning, memory, and synaptic plasticity. J. Neurosci. *26*, 1844–1853.

Hauck, B., Chen, L., and Xiao, W. (2003). Generation and characterization of chimeric recombinant AAV vectors. Mol. Ther. *7*, 419–425.

Hazra, A., Gu, F., Aulakh, A., Berridge, C., Eriksen, J.L., and Ziburkus, J. (2013). Inhibitory neuron and hippocampal circuit dysfunction in an aged mouse model of Alzheimer's disease. PLoS ONE *8*, e64318.

Hengen, K.B., Torrado Pacheco, A., McGregor, J.N., Van Hooser, S.D., and Turrigiano, G.G. (2016). Neuronal firing rate homeostasis is inhibited by sleep and promoted by wake. Cell *165*, 180–191.

Hines, M.L., and Carnevale, N.T. (2003). The NEURON simulation environment. In The Handbook of Brain Theory and Neural Networks, *Volume 2*, M.A. Arbib, ed. (MIT Press), pp. 769–773.

Holsinger, R.M.D., McLean, C.A., Beyreuther, K., Masters, C.L., and Evin, G. (2002). Increased expression of the amyloid precursor beta-secretase in Alzheimer's disease. Ann. Neurol. *51*, 783–786.

Hoxha, E., Boda, E., Montarolo, F., Parolisi, R., and Tempia, F. (2012). Excitability and synaptic alterations in the cerebellum of APP/PS1 mice. PLoS ONE *7*, e34726.

Jonsson, T., Atwal, J., Steinberg, S., Snaedal, J., Jonsson, P., Bjornsson, S., Stefansson, H., Sulem, P., Gudbjartsson, D., Maloney, J., et al. (2012). A mutation in APP protects against Alzheimer's disease and age-related cognitive decline. Nature *488*, 96–99.

Kaczorowski, C.C., Sametsky, E., Shah, S., Vassar, R., and Disterhoft, J.F. (2011). Mechanisms underlying basal and learning-related intrinsic excitability in a mouse model of Alzheimer's disease. Neurobiol. Aging *32*, 1452–1465.

Kerrigan, T.L., Brown, J.T., and Randall, A.D. (2014). Characterization of altered intrinsic excitability in hippocampal CA1 pyramidal cells of the Aβ-overproducing PDAPP mouse. Neuropharmacology *79*, 515–524.

Kimberly, W.T., Zheng, J.B., Guénette, S.Y., and Selkoe, D.J. (2001). The intracellular domain of the beta-amyloid precursor protein is stabilized by Fe65 and translocates to the nucleus in a notch-like manner. J. Biol. Chem. *276*, 40288–40292.

King, B., Rizwan, A.P., Asmara, H., Heath, N.C., Engbers, J.D.T., Dykstra, S., Bartoletti, T.M., Hameed, S., Zamponi, G.W., and Turner, R.W. (2015). IKCa channels are a critical determinant of the slow AHP in CA1 pyramidal neurons. Cell Rep. *11*, 175–182.

Klevanski, M., Herrmann, U., Weyer, S.W., Fol, R., Cartier, N., Wolfer, D.P., Caldwell, J.H., Korte, M., and Müller, U.C. (2015). The APP intracellular domain

is required for normal synaptic morphology, synaptic plasticity, and hippocampus-dependent behavior. J. Neurosci. *35*, 16018–16033.

Köhler, M., Hirschberg, B., Bond, C.T., Kinzie, J.M., Marrion, N.V., Maylie, J., and Adelman, J.P. (1996). Small-conductance, calcium-activated potassium channels from mammalian brain. Science *273*, 1709–1714.

Konietzko, U. (2012). AICD nuclear signaling and its possible contribution to Alzheimer's disease. Curr. Alzheimer Res. *9*, 200–216.

Kumar, A., and Foster, T.C. (2002). 17beta-estradiol benzoate decreases the AHP amplitude in CA1 pyramidal neurons. J. Neurophysiol. *88*, 621–626.

Lancaster, B., and Nicoll, R.A. (1987). Properties of two calcium-activated hyperpolarizations in rat hippocampal neurones. J. Physiol. *389*, 187–203.

Lancaster, B., and Zucker, R.S. (1994). Photolytic manipulation of Ca^{2+} and the time course of slow, Ca^{2+}-activated K^+ current in rat hippocampal neurones. J. Physiol. *475*, 229–239.

Landfield, P.W., and Pitler, T.A. (1984). Prolonged Ca^{2+}-dependent afterhyperpolarizations in hippocampal neurons of aged rats. Science *226*, 1089–1092.

Lauritzen, I., Pardossi-Piquard, R., Bauer, C., Brigham, E., Abraham, J.D., Ranaldi, S., Fraser, P., St-George-Hyslop, P., Le Thuc, O., Espin, V., et al. (2012). The β-secretase-derived C-terminal fragment of βAPP, C99, but not Aβ, is a key contributor to early intraneuronal lesions in triple-transgenic mouse hippocampus. J. Neurosci. *32*, 16243–16255.

Leissring, M.A., Murphy, M.P., Mead, T.R., Akbari, Y., Sugarman, M.C., Jannatipour, M., Anliker, B., Müller, U., Saftig, P., De Strooper, B., et al. (2002). A physiologic signaling role for the gamma -secretase-derived intracellular fragment of APP. Proc. Natl. Acad. Sci. USA *99*, 4697–4702.

Lisman, J.E., and Idiart, M.A. (1995). Storage of 7 +/− 2 short-term memories in oscillatory subcycles. Science *267*, 1512–1515.

Madison, D.V., and Nicoll, R.A. (1984). Control of the repetitive discharge of rat CA 1 pyramidal neurones in vitro. J. Physiol. *354*, 319–331.

Marcantoni, A., Raymond, E.F., Carbone, E., and Marie, H. (2014). Firing properties of entorhinal cortex neurons and early alterations in an Alzheimer's disease transgenic model. Pflugers Arch. *466*, 1437–1450.

Marie, H., Morishita, W., Yu, X., Calakos, N., and Malenka, R.C. (2005). Generation of silent synapses by acute in vivo expression of CaMKIV and CREB. Neuron *45*, 741–752.

Marrion, N.V., and Tavalin, S.J. (1998). Selective activation of Ca^{2+}-activated K^+ channels by co-localized Ca^{2+} channels in hippocampal neurons. Nature *395*, 900–905.

Minkeviciene, R., Rheims, S., Dobszay, M.B., Zilberter, M., Hartikainen, J., Fülöp, L., Penke, B., Zilberter, Y., Harkany, T., Pitkänen, A., and Tanila, H. (2009). Amyloid beta-induced neuronal hyperexcitability triggers progressive epilepsy. J. Neurosci. *29*, 3453–3462.

Moyer, J.R., Jr., Power, J.M., Thompson, L.T., and Disterhoft, J.F. (2000). Increased excitability of aged rabbit CA1 neurons after trace eyeblink conditioning. J. Neurosci. *20*, 5476–5482.

Nalivaeva, N.N., and Turner, A.J. (2017). Role of ageing and oxidative stress in regulation of amyloid-degrading enzymes and development of neurodegeneration. Curr. Aging Sci. *10*, 32–40.

Núñez-Santana, F.L., Oh, M.M., Antion, M.D., Lee, A., Hell, J.W., and Disterhoft, J.F. (2014). Surface L-type Ca^{2+} channel expression levels are increased in aged hippocampus. Aging Cell *13*, 111–120.

Palop, J.J., Chin, J., Roberson, E.D., Wang, J., Thwin, M.T., Bien-Ly, N., Yoo, J., Ho, K.O., Yu, G.-Q., Kreitzer, A., et al. (2007). Aberrant excitatory neuronal activity and compensatory remodeling of inhibitory hippocampal circuits in mouse models of Alzheimer's disease. Neuron *55*, 697–711.

Pardossi-Piquard, R., and Checler, F. (2012). The physiology of the β-amyloid precursor protein intracellular domain AICD. J. Neurochem. *120* (*Suppl 1*), 109–124.

Pastorino, L., Sun, A., Lu, P.J., Zhou, X.Z., Balastik, M., Finn, G., Wulf, G., Lim, J., Li, S.H., Li, X., et al. (2006). The prolyl isomerase Pin1 regulates amyloid precursor protein processing and amyloid-beta production. Nature *440*, 528–534.

Peron, S., and Gabbiani, F. (2009). Spike frequency adaptation mediates looming stimulus selectivity in a collision-detecting neuron. Nat. Neurosci. *12*, 318–326.

Pousinha, P.A., Mouska, X., Raymond, E.F., Gwizdek, C., Dhib, G., Poupon, G., Zaragosi, L.-E., Giudici, C., Bethus, I., Pacary, E., et al. (2017). Physiological and pathophysiological control of synaptic GluN2B-NMDA receptors by the C-terminal domain of amyloid precursor protein. eLife *6*, e25659.

Power, J.M., Wu, W.W., Sametsky, E., Oh, M.M., and Disterhoft, J.F. (2002). Age-related enhancement of the slow outward calcium-activated potassium current in hippocampal CA1 pyramidal neurons in vitro. J. Neurosci. *22*, 7234–7243.

Rose, G.M., Ong, V.S., and Woodruff-Pak, D.S. (2007). Efficacy of MEM 1003, a novel calcium channel blocker, in delay and trace eyeblink conditioning in older rabbits. Neurobiol. Aging *28*, 766–773.

Sah, P. (1996). Ca^{2+}-activated K^+ currents in neurones: types, physiological roles and modulation. Trends Neurosci. *19*, 150–154.

Sahu, G., Asmara, H., Zhang, F.-X., Zamponi, G.W., and Turner, R.W. (2017). Activity-dependent facilitation of $Ca_V1.3$ calcium channels promotes KCa3.1 activation in hippocampal neurons. J. Neurosci. *37*, 11255–11270.

Santos, S.F., Pierrot, N., Morel, N., Gailly, P., Sindic, C., and Octave, J.-N. (2009). Expression of human amyloid precursor protein in rat cortical neurons inhibits calcium oscillations. J. Neurosci. *29*, 4708–4718.

Santos, S.F., Tasiaux, B., Sindic, C., and Octave, J.-N. (2011). Inhibition of neuronal calcium oscillations by cell surface APP phosphorylated on T668. Neurobiol. Aging *32*, 2308–2313.

Schmittgen, T.D., and Livak, K.J. (2008). Analyzing real-time PCR data by the comparative C(T) method. Nat. Protoc. *3*, 1101–1108.

Selkoe, D.J. (2002). Alzheimer's disease is a synaptic failure. Science *298*, 789–791.

Slomowitz, E., Styr, B., Vertkin, I., Milshtein-Parush, H., Nelken, I., Slutsky, M., and Slutsky, I. (2015). Interplay between population firing stability and single neuron dynamics in hippocampal networks. eLife *4*, e04378.

Stam, C.J., van Cappellen van Walsum, A.M., Pijnenburg, Y.A.L., Berendse, H.W., de Munck, J.C., Scheltens, P., and van Dijk, B.W. (2002). Generalized synchronization of MEG recordings in Alzheimer's disease: evidence for involvement of the gamma band. J. Clin. Neurophysiol. *19*, 562–574.

Storm, J.F. (1987). Action potential repolarization and a fast after-hyperpolarization in rat hippocampal pyramidal cells. J. Physiol. *385*, 733–759.

Storm, J.F. (1990). Potassium currents in hippocampal pyramidal cells. Prog. Brain Res. *83*, 161–187.

Trimper, J.B., Galloway, C.R., Jones, A.C., Mandi, K., and Manns, J.R. (2017). Gamma oscillations in rat hippocampal subregions dentate gyrus, CA3, CA1, and subiculum underlie associative memory encoding. Cell Rep. *21*, 2419–2432.

Turner, R.W., Asmara, H., Engbers, J.D.T., Miclat, J., Rizwan, A.P., Sahu, G., and Zamponi, G.W. (2016). Assessing the role of IKCa channels in generating the sAHP of CA1 hippocampal pyramidal cells. Channels (Austin) *10*, 313–319.

Valadas, J.S., Batalha, V.L., Ferreira, D.G., Gomes, R., Coelho, J.E., Sebastião, A.M., Diógenes, M.J., and Lopes, L.V. (2012). Neuroprotection afforded by adenosine A2A receptor blockade is modulated by corticotrophin-releasing factor (CRF) in glutamate injured cortical neurons. J. Neurochem. *123*, 1030–1040.

van der Kant, R., and Goldstein, L.S. (2015). Cellular functions of the amyloid precursor protein from development to dementia. Dev. Cell *32*, 502–515.

Velumian, A.A., and Carlen, P.L. (1999). Differential control of three after-hyperpolarizations in rat hippocampal neurones by intracellular calcium buffering. J. Physiol. *517*, 201–216.

Veng, L.M., Mesches, M.H., and Browning, M.D. (2003). Age-related working memory impairment is correlated with increases in the L-type calcium channel protein alpha1D (Cav1.3) in area CA1 of the hippocampus and both are ameliorated by chronic nimodipine treatment. Brain Res. Mol. Brain Res. *110*, 193–202.

Verret, L., Mann, E.O., Hang, G.B., Barth, A.M.I., Cobos, I., Ho, K., Devidze, N., Masliah, E., Kreitzer, A.C., Mody, I., et al. (2012). Inhibitory interneuron deficit links altered network activity and cognitive dysfunction in Alzheimer model. Cell *149*, 708–721.

Villalobos, C., Shakkottai, V.G., Chandy, K.G., Michelhaugh, S.K., and Andrade, R. (2004). SKCa channels mediate the medium but not the slow calcium-activated afterhyperpolarization in cortical neurons. J. Neurosci. *24*, 3537–3542.

Wuytack, F., Raeymaekers, L., and Missiaen, L. (2002). Molecular physiology of the SERCA and SPCA pumps. Cell Calcium *32*, 279–305.

Wykes, R., Kalmbach, A., Eliava, M., and Waters, J. (2012). Changes in the physiology of CA1 hippocampal pyramidal neurons in preplaque CRND8 mice. Neurobiol. Aging *33*, 1609–1623.

Zhang, W., and Linden, D.J. (2003). The other side of the engram: experience-driven changes in neuronal intrinsic excitability. Nat. Rev. Neurosci. *4*, 885–900.

Zheng, C., Bieri, K.W., Hwaun, E., and Colgin, L.L. (2016). Fast gamma rhythms in the hippocampus promote encoding of novel object-place pairings. eNeuro *3*, ENEURO.0001-16.2016.

STAR★METHODS

KEY RESOURCES TABLE

REAGENT or RESOURCE	SOURCE	IDENTIFIER
Chemicals, Peptides, and Recombinant Proteins		
TAT-AICDnls: YGRKKRRQRRRVMLKKKQYT SIHHGVVEVDAA VTPEERHLSKMQQNGYENPTYKFFEQMQNPKKKRKV	PSL GmbH (Heidelberg, Germany)	N/A
TAT-scrAICDnls: YGRKKRRQRRRVQGITQKMYHNQEGKF LNQKVNVKTHMQFEHETLVDSMKAYYRVEEPSAPKKKRKV	PSL GmbH (Heidelberg, Germany)	N/A
Actinomycin	Sigma	Cat#A9415
Apamin	Calbiochem	CAS 24345-16-2
TRAM-34	Abcam	Cat# ab141885
D-APV	Abcam	Cat# ab120003
TTX	Abcam	Cat# ab120055
nimodipine	Abcam	Cat# ab120138
Isradipine	Abcam	Cat# ab120142
Critical Commercial Assays		
RNeasy Plus Mini Kit	QIAGEN, Germany	Cat# 74134
SuperScript First-Strand Synthesis System	Invitrogen, USA	Cat# 18091050
Power SYBR Green PCR Master Mix	Applied Biosystems, UK	Cat#1725095
Deposited Data		
CA1 pyramidal neuron model	Bianchi et al., 2014	ModelDB acc.n.151126
All models and simulation files for this paper	This paper	https://senselab.med.yale.edu/ModelDB, acc.n. 256388
Experimental Models: Cell Lines		
AAV-293 cells	Agilent Technologies, USA	RRID:CVCL_6871
Experimental Models: Organisms/Strains		
Rat: Sprague Dawley	Janvier Labs, France	RRID:RGD:5508397
Mouse: C57BL/6JRj	Janvier Labs, France	*RRID:MGI:5752053*
Oligonucleotides		
PPIA peptidylprolyl isomerase A (cyclophilin A) Forward Primer: ATCTGCACTGCCAAGACTGAGTG	Invitrogen, USA	N/A
PPIA peptidylprolyl isomerase A (cyclophilin A) Reverse Primer: CTTCTTGCTGGTCTTGCCATTCC	Invitrogen, USA	N/A
Ribosomal protein L13A Forward Primer: GGATCCCTCCACCCTATGACA	Invitrogen, USA	N/A
Ribosomal protein L13A Reverse Primer: CTGGTACTTCCACCCGACCTC	Invitrogen, USA	N/A
Potassium Calcium-Activated Channel Subfamily N Member 2 Forward Primer: TATGCGCTCATCTTCGGCAT	Invitrogen, USA	N/A
Potassium Calcium-Activated Channel Subfamily N Member 2 Reverse Primer: AGAATACAGCGACGCCTTGT	Invitrogen, USA	N/A
Potassium Calcium-Activated Channel Subfamily N Member 4 Forward Primer: AGTGTTTAATCACGCTGTCCACT	Invitrogen, USA	N/A
Potassium Calcium-Activated Channel Subfamily N Member 4 Reverse Primer: CCCGTTGTCAGTCATGAACA	Invitrogen, USA	N/A
Calcium voltage-gated channel subunit alpha1 C Forward Primer: TGCCTCCGAACACTACAACC	Invitrogen, USA	N/A
Calcium voltage-gated channel subunit alpha1 C Reverse Primer: CCCCGCACACAATGAAACAG	Invitrogen, USA	N/A

(*Continued on next page*)

Continued

REAGENT or RESOURCE	SOURCE	IDENTIFIER
Recombinant DNA		
AAV helper DNA: pH21	Hauck et al., 2003	N/A
AAV helper DNA: pRV1	Hauck et al., 2003	N/A
AAV helper DNA: pF6	Hauck et al., 2003	N/A
pAAV-IRES-hrGFP	Agilent Technologies, USA	Cat#240075
pAAV-AICD-IRES-hrGFP	Pousinha et al., 2017	N/A
pAAV-AICD-NLS-IRES-hrGFP	Pousinha et al., 2017	Addgene: #107543
pAAV-AICD-NES-IRES-hrGFP	Pousinha et al., 2017	Addgene: #107544
pAAV-syn-IRES-hrGFP	Pousinha et al., 2017	Addgene: #107549
pAAV-syn-AICD-IRES-hrGFP	Pousinha et al., 2017	Addgene: #107548

LEAD CONTACT AND MATERIALS AVAILABILITY

Further information and requests for resources and reagents should be directed to and will be fulfilled by the Lead Contact, Paula A. Pousinha (pousinha@ipmc.cnrs.fr).

Some Plasmids used in this study are available in Addgene [pAAV-AICD-NLS-IRES-hrGFP, Addgene: #107543; pAAV-AICD-NES-IRES-hrGFP, Addgene: #107544; pAAV-syn-IRES-hrGFP, Addgene: #107549; pAAV-syn-AICD-IRES-hrGFP, Addgene: #107548].

All unique/stable reagents generated in this study are available from the Lead Contact without restriction.

EXPERIMENTAL MODEL AND SUBJECT DETAILS

Animals

Sprague Dawley male rats (RRID:RGD_5508397) (Janvier Labs, France) were used at post-natal days (PND) 21-30. Male C57BL/6JRj mice (Janvier Labs, France) were used at 8-12 weeks of age. All experiments were done according to policies on the care and use of laboratory animals of European Communities Council Directive (2010/63). The protocols were approved by the French Research Ministry following evaluation by a specialized ethics committee (protocol number 00973.02 and 00468.03). All efforts were made to minimize animal suffering and reduce the number of animals used. The animals were housed three per cage under controlled laboratory conditions with a 12-h dark light cycle, a temperature of 22 ± 2°C. Animals had free access to standard rodent diet and tap water.

Primary neuronal cultures

Cortical and hippocampal neurons were cultured from 18 day Sprague Dawley rat embryos (Harlan, Barcelona, Spain) as previously described (Valadas et al., 2012). Briefly, embryos were collected in Hank's Balanced Salt Solution (HBSS, Corning, USA) and rapidly decapitated. Meninges were removed, and whole cortices (hippocampi and attached cortex) were dissociated and incubated for 15 min in HBSS with 0.025% trypsin. Cells were washed once with HBSS with 30% Fetal Bovine Serum (FBS), centrifuged three times, re-suspended in Neurobasal Medium (GIBCO – Life Technologies, USA) supplemented with 2% B-27 supplement, 25 μM Glutamate, 0.5 mM glutamine, and 2 U/ml Penicillin/Streptomycin, gently dissociated and filtered through a 70 μm strainer (VWR, USA). Cells were plated on poly-D-lysine-coated plates and grown for 14 days at 37°C in a 5% CO2-humidified atmosphere in the previously described supplemented Neurobasal medium, in the absence of any positive selection for neurons. Day 12-14, neurons were treated with TAT-scrAICDnls or TAT-AICDnls (100 nM) for 2 h and proceed to RNA extraction.

METHOD DETAILS

Virus Constructs

Virus cloning

c-DNA encoding a methionine followed by the last 50 amino acids of human βAPP without or with the SV40 nuclear localization signal (NLS; PKKKRKV) or the HIV-1 Rev nuclear export signal (NES: LPPLERLTL) attached to its C-terminal end, called AICD and AICDnls and AICDnes respectively, were inserted into the multiple cloning site (MCS) of the pAAV-IRES-hrGFP vector (Agilent Technologies, USA) by standard PCR cloning. Empty pAAV-IRES-hrGFP vector expressing only GFP was used as control (referred to as GFP virus) (Pousinha et al., 2017). High titer synGFP and synAICD viruses were constructed using the backbone vector pAAV-syn-GFP (Addgene plasmid #58867). In this vector, the GFP cDNA was replaced by either the hrGFP or the AICD-IRES-hrGFP using standard PCR cloning.

Virus Production

GFP, AICD, AICDnls and AICDnes recombinant AAV virions, all expressing hrGFP, were produced essentially as described previously (Hauck et al., 2003; Pousinha et al., 2017). Briefly, to produce rAAV virions containing 1:1 ratio of type 1 and type 2 capsid proteins, AAV-293 cells (Agilent Technologies, USA) were co-transfected with the GFP, AICD, AICDnls, AICDnes plasmid and three helper plasmids (pH21, pRV1 and pF6) using the calcium phosphate method. 65 h post-transfection, the cells were harvested, rAAVs were purified using 1 mL HiTrap heparin columns (Sigma-Aldrich, France) and concentrated using Amicon Ultra centrifugal filter devices (Millipore, USA). The concentrated viral solution was aliquoted and stored at −80°C until further use. Titer quantification was performed in HT1080 cells as described by Agilent Technologies. We consistently obtained titers of ~5 × 108 particles/ml for viruses for viruses exhibiting low transduction efficiency (GFP, AICD, AICDnls, AICDnes) and ~5 × 1012 particles/ml for viruses with high transduction efficiency (synGFP and synAICD).

TAT peptides

TAT-scrAICDnls and TAT-AICDnls were synthesized by PSL GmbH (Heidelberg, Germany). TAT-AICDnls contained the TAT sequence (YGRKKRRQRRR), conferring cell permeability, fused to the N-terminal of AICD:

MLKKKQYTSIHHGVVEVDAAVTPEERHLSKMQQNGYENPTYKFFEQMQN. The SV40 nuclear localization signal (NLS; PKKKRKV) was added to the AICD C-terminal for nuclear translocation. The TAT-scr AICDnls contained the same TAT and NLS sequences at each end of a scrambled version of the AICD sequence: VQGITQKMYHNQEGKFLNQKVNVKTHMQFEHETLVDSMKAYYRVEEPSPA. The purity of peptides was above 90%–95%.

In Vivo AAV Injections

PND21-22 Sprague Dawley male rats (50-70 g) were anesthetized with a mixture of ketamine (0.2 mg/g body weight) and xylazine (0.04 mg/g body weight) by intraperitoneal injection. Local analgesia was increased by injecting 35-40 μl of lidocaine (diluted at 0.5%) at site of incision. After immobilization on a stereotaxic instrument, a hole per hemisphere side was drilled (1-2 mm diameter) at −4 mm posterior and ± 2.5 mm lateral to bregma for injection in the CA1 region of the hippocampus. Using a stainless steel canula at a depth of 2.6 mm, viral solution (1 μl) was injected with a Harvard Apparatus pump at a flow rate of 0.2 μl/min. Rats were sutured and Ketofen (diluted in the bottle of water, 5mg/L) was administrated during the first 24h after surgery to ease post-operative pain.

C57BL/6JRj mice of 8 weeks' old were injected with either synGFP AAV and synAICD AAV in both dorsal hippocampi. Stereotaxic injections were performed using a stereotaxic frame (Kopf Instruments) under general anesthesia with xylazine and ketamine (10 mg/kg and 150 mg/kg, respectively). 500nl of synGFP or synAICD were injected in each hippocampus with an injection rate set at 100nl/min. Coordinates for dorsal hippocampus were adjusted from Paxinos and Watson (AP: −2,2, ML ± 1,5, DV −1,4). After injection, animals were stitched and a 3 weeks' recovery period were given to allow sufficient viral expression.

Quantitative PCR in primary neuronal cultures

RNA extraction and quantitative real-time PCR analysis (RT-qPCR): Total RNA was extracted and purified using the RNeasy Plus Mini Kit (QIAGEN, Germany). RNA quality was assessed by NanoDrop 2000 (Thermo Scientific, USA) analysis (A260/A280 ≈2; 260/235 > 1.8). Total RNA (2 μg) was reverse-transcribed using random primers and SuperScript First-Strand Synthesis System for RT-PCR (Invitrogen, USA). RT-qPCR analysis was performed on a Corbett Rotor-gene 6000 apparatus (QIAGEN, Germany) using Power SYBR Green PCR Master Mix (Applied Biosystems, UK), 0.2 μM of each primer and 1/20 dilutions of total cDNA (final concentration 0.4 ng/μl). The thermal cycler conditions were 10 min at 95°C, 40 cycles of a two-step PCR, 95°C for 15 s followed by 60°C for 25 s with a final thermal ramp from 72 to 95°C. Primer efficiencies (E = 1 ± 0.02) were obtained from standard curves of serial dilutions (slope and R2 respectively around −3.3 and 0.99). Sequences of primers used (all from Invitrogen, UK, HPLC purified) are listed in Figure S3. Reference genes were PPIA (cyclophilin A) and Rpl13A (ribosomal protein L13A). Amplifications were carried out in triplicate in two independent runs, and according to the MIQE guidelines (Bustin et al., 2009). The relative expression of target genes was determined by the comparative CT method (Schmittgen and Livak, 2008).

Pharmacological tools

Different pharmacological tools were used: Actinomycin (Sigma Aldrich, France) to inhibit gene transcription, Apamin (Calbiochem, France) to block SK channels, TRAM-34 to block KCa3.1 channels (Abcam, France); D-AP5 (abcam, France) to block NMDA receptors, TTX (abcam, France) to block voltage-gated Na^+ channels, nimodipine (abcam, France) and Isradipine (Abcam, France) to block L-type Ca^{2+} channels.

Patch-Clamp Electrophysiology

Electrophysiological recordings were done on rats or mice 12-20 days after *in vivo* viral injections or on naive rats (PND32-40). Acute transverse hippocampal slices (250 μm thick) were prepared using standard procedures (Marie et al., 2005), resumed in the Supplement.

Slices were visualized on an upright microscope with IR-DIC illumination and epi-fluorescence (Scientifica, Ltd). Whole-cell recordings were performed using a Multiclamp 700B (Molecular Devices) amplifier, under the control of pClamp10 software (Molecular Devices).

After a tight seal (> 1GΩ) on the cell body of the selected neuron was obtained, whole-cell patch clamp configuration was established, and cells were left to stabilize for 2-3 min before recordings began. Holding current and series resistance were continuously monitored throughout the experiment, and if either of these two parameters varied by more than 20%, the experiment was discarded.

Brain slices preparation

Briefly, rats were anaesthized with isoflurane and decapitated. Hippocampi were quickly removed. slices were cut on a vibratome (Microm HM600V, Thermo Scientific) in ice-cold dissecting solution containing (in mM): 234 sucrose, 2.5 KCl, 0.5 CaCl2, 10 MgCl2, 26 NaHCO3, 1.25 NaH2PO4 and 11 D-glucose, oxygenated with 95% O2 and 5% CO2, pH 7.4. Slices were first incubated, for 60 min at 37°C, in an artificial CSF (aCSF) solution containing (in mM): 119 NaCl, 2.5 KCl, 1.25 NaH2PO4, 26 NaHCO3, 1.3 MgSO4, 2.5 CaCl2 and 11 D-glucose, oxygenated with 95% O2 and 5% CO2, pH 7.4. Slices were used after recovering for another 30 min at room temperature. For all experiments, slices were perfused with the oxygenated aCSF at 31 ± 1°C. In the case of AICD ex-vivo delivery, slices were pre-incubated in TAT peptides for 2h to 5h. Control (scramble AICD) and TAT-AICD peptides were tested in parallel. Recording pipettes (5-6 MΩ) for voltage-clamp experiments were filled with a solution containing the following (in mM): 117.5 Cs-gluconate, 15.5 CsCl, 10 TEACl, 8 NaCl, 10 HEPES, 0.25 EGTA, 4 MgATP and 0.3 NaGTP (pH 7.3; osmolarity 290-300 mOsm). For current-clamp experiments, the recording pipette solution contained (in mM): 135 gluconic acid (potassium salt: K-gluconate), 5 NaCl, 2 MgCl2, 10 HEPES, 0.5 EGTA, 2 MgATP and 0.4 NaGTP (pH 7.25; osmolarity 280-290 mOsm).

Electrophysiology Protocols

The resting membrane potential (Vm) was first measured in the absence of any spontaneous firing, and only cells more negative than −55 mV were considered. The membrane resistance was obtained by clamping neurons at Vh = −60 mV, injecting −200pA of current (500ms duration), measuring the amount of steady-state hyperpolarization and calculating the resistance value by Ohm's law (Figure S1).

To study the relationship between firing frequency and current input (e.g., Figures 1D and 1F), we first adjusted the membrane potential (Vh) to −65 mV and then injected pulses of increased intensity in steps of 50 pA (from 100 to 600 pA, 200 ms duration). In the case of pharmacological studies on neuron firing frequency (Figures 1H, 3B, 3G, 4A, and S3A), drugs were added to the perfusion bath at least 30 min before recordings.

The involvement of Na^+ channels in spike generation was derived from "phase-plane" plot obtained by drawing the first time derivative of voltage (dV/dt) versus voltage (Figure S2). We could thus estimate the amount of transient Na^+ current contributing to the spike up-stroke from the maximal value of dV/dt (dV/dtmax) and the spike threshold as the voltage at which dV/dt was 4% of dV/dtmax (Bean, 2007). We restricted the analysis of Na^+ channel availability in spike generation by considering only the action potentials (APs) generated at I = 500pA, a current step inducing a significant difference in the firing frequency between AICD neurons and respective controls.

We measured the spike-frequency adaptation for I = 500pA as the ratio between the ratio between the last AP inter-stimulus interval (ISI) and the first AP ISI (Figure 1E).

AHPs were triggered by a high-frequency train of APs that consisted of 12 APs at 60Hz and were reported as an average of 2 sweeps per cell. The mAHP amplitude was defined as the difference between the membrane potential at the beginning (before cell depolarization) and the peak negative value 20 – 100 ms following the train of APs (Figure 2A). The sAHP amplitude was defined as the as the difference between the membrane potential at the beginning (before cell depolarization) and the peak negative value at 400ms following the train of APs. The sAHP area was defined as the area within 400ms to 4 s following the train of APs.

For measurement of the IAHP, TTX was added to the bath solution. Neurons were voltage clamped at −55 mV, and tail currents were evoked with a depolarizing step to +20 mV for 100ms followed by a return to −55 mV (Hammond et al., 2006) (Figure 3C). After a stable line was established, apamin (100nM) was applied to the bath. The apamin sensitive current (ISK) was obtained by subtraction of the IAHP obtained before and after 30 min of apamin application (Figures 3D and 3E).

For mesurements of the nimodipine-sensitive currents, TTX and Picrotoxin were added to the bath solution. Neurons were voltage clamped at −60 mV, and tail currents were evoked with a hyperpolarizing step to −100 mV for 100ms followed by 200 ms depolarizing current pulses, incrementing in steps of 10pA and return to −60 mV. The nimodipine sensitive current was obtained by subtraction of the current obtained before and 30 min after nimodipine application (Figures 4D–4F).

In silico modeling

All simulations were carried out using the NEURON environment (v7.6, Hines and Carnevale 2003) and a CA1 pyramidal neuron implemented with the simplified 15-compartments morphology taken from Bianchi et al. (2014) (ModelDB acc.n.151126). All models and simulation files will be uploaded to the public ModelDB database (https://senselab.med.yale.edu/ModelDB, acc.n. 256388).

The model neuron included Hodgkin-Huxley type currents (axon and somadendritic, Na^+ and Kdr), two A-type potassium current (proximal and distal dendrites), one M-type potassium current, a h-current, three types of voltage dependent calcium currents (CaL, CaT, CaR), two types of calcium dependent potassium current (a slow AHP and a medium AHP current) and a calcium pump. The channel peak conductances and the dendrites diameters and lengths were modified from their original values (tuned to be consistent with recordings in mice), to take into account the specific set of experimental recordings in mice used in this work. We implemented two main excitatory synaptic afferent pathways, as in Bianchi et al. (2014): one mimiking EC inputs (20 AMPA synapses, each one

with a peak conductance of 1.45nS) and another one modeling CA3 Schaffer collateral inputs (20 AMPA and NMDA synapses, with peak conductances 1.45 and 0.5nS, respectively). Each synapse was independently activated according to a Poisson distribution, at an average frequency of 40 Hz (in the γ range).

Behavioral analysis

42 Sprague Dawley male rats were tested in a spatial object recognition task at P32, 15 days after *in vivo* virus transduction by stereotaxic surgery.

Experiments were performed during day (9h-18h). A plexiglass square openfield of 60 cm with cues on the wall was used. Linoleum was placed on the floor. Objects for Sample and Test were similar (plastic, ~15 cm high and ~10 cm large). The floor was cleaned with 10% ethanol solution and rinse with water between each trial. The intensity of the light was set at 4 lux to minimize anxiety. We adapted a behavioral protocol that was previously described to test spatial memory (Zheng et al., 2016), which consisted of two trials with 5 min duration with 20 min inter-trial interval (ITI). First, rats were allowed to freely explore the apparatus for two consecutive days during 5 min (Habituation). Then, rats were submitted to a Pre-training, where two different objects, which were not reused in the test day, were placed in the arena in a constant location, to minimize neophobia. On the Test day, animals were allowed to explore two new identical objects in a first trial (Sample Trial). After the 20 min ITI, for the Test trial, the same objects were presented, but one object was presented in a new location (Displaced object), while the other object remained in its previous location (Non-displaced object). Object configurations for Sample and Test trials were counter-balanced. Experiments and analysis were done blind as to condition (SynGFP- or synAICD transduced rats). Object exploration was scored only when the animal was facing an object, with its nose within 1 cm of the object. Moments when the rat was touching the object with another part of the body, or when leaning or rearing on the object were not scored as object exploration. For the Test trial, a discrimination index was calculated: [time spent exploring object in the novel location]/[total objects exploring time]. The index value is ~0.5 (chance value) if the animal does not show any object preference, spending similar time exploring each object. The trajectory of the animals was video recorded and tracked with ANYmaze software (Stoelting, Wood Dale, USA). The total distance traveled (presented as 1 min bins) and average speeds during Test trial were counted as measures of locomotor activity. The analysis of thigmotaxis, a measure of anxiety, was calculated as the time spent in center compared to the time spent in the periphery of the apparatus. At the end of the behavioral experiments, all brains were dissected and correct targeting of the hippocampus was verified (GFP fluorescence). Two AICD injected rats were removed from the analysis due to misplaced viral injections.

QUANTIFICATION AND STATISTICAL ANALYSES

Results are shown as mean ± SEM 'n' refers to the number of cells examined, unless otherwise stated. Statistical significance of differences between means was determined through Prism 6.0 software (GraphPad) and is presented in details in the Supplement (Tables S1, S2, S3, S4, S5, and S6). Significance was taken at $p < 0.05$. the Student's t test or the Wilcoxon test were performed whenever two conditions were compared, according to the samples distribution normality. One factor analysis of variance (ANOVA) was performed to analyze significance among the different conditions. In experiments where mean firing frequency was analyzed as a function of injected current, a Two-way ANOVA with repeated-measures was applied. In studies where two variables were tested (e.g., drugs and virus, or behavioral analysis) a Two-way ANOVA was performed. For behavioral analysis, the discrimination index of each group was compared to chance performance (score of 0.5) using one sample t tests (two-tailed).

DATA AND CODE AVAILABILITY

All simulation and model files are available for public download on the ModelDB repository (acc.n.256388).

Cell Reports, Volume *29*

Supplemental Information

The Amyloid Precursor Protein C-Terminal Domain Alters CA1 Neuron Firing, Modifying Hippocampus Oscillations and Impairing Spatial Memory Encoding

Paula A. Pousinha, Xavier Mouska, Daniela Bianchi, Mariana Temido-Ferreira, Joana Rajão-Saraiva, Rui Gomes, Sebastian P. Fernandez, Ana Rita Salgueiro-Pereira, Carine Gandin, Elisabeth F. Raymond, Jacques Barik, Romain Goutagny, Ingrid Bethus, Luisa V. Lopes, Michele Migliore, and Hélène Marie

SUPPLEMENTAL FIGURES

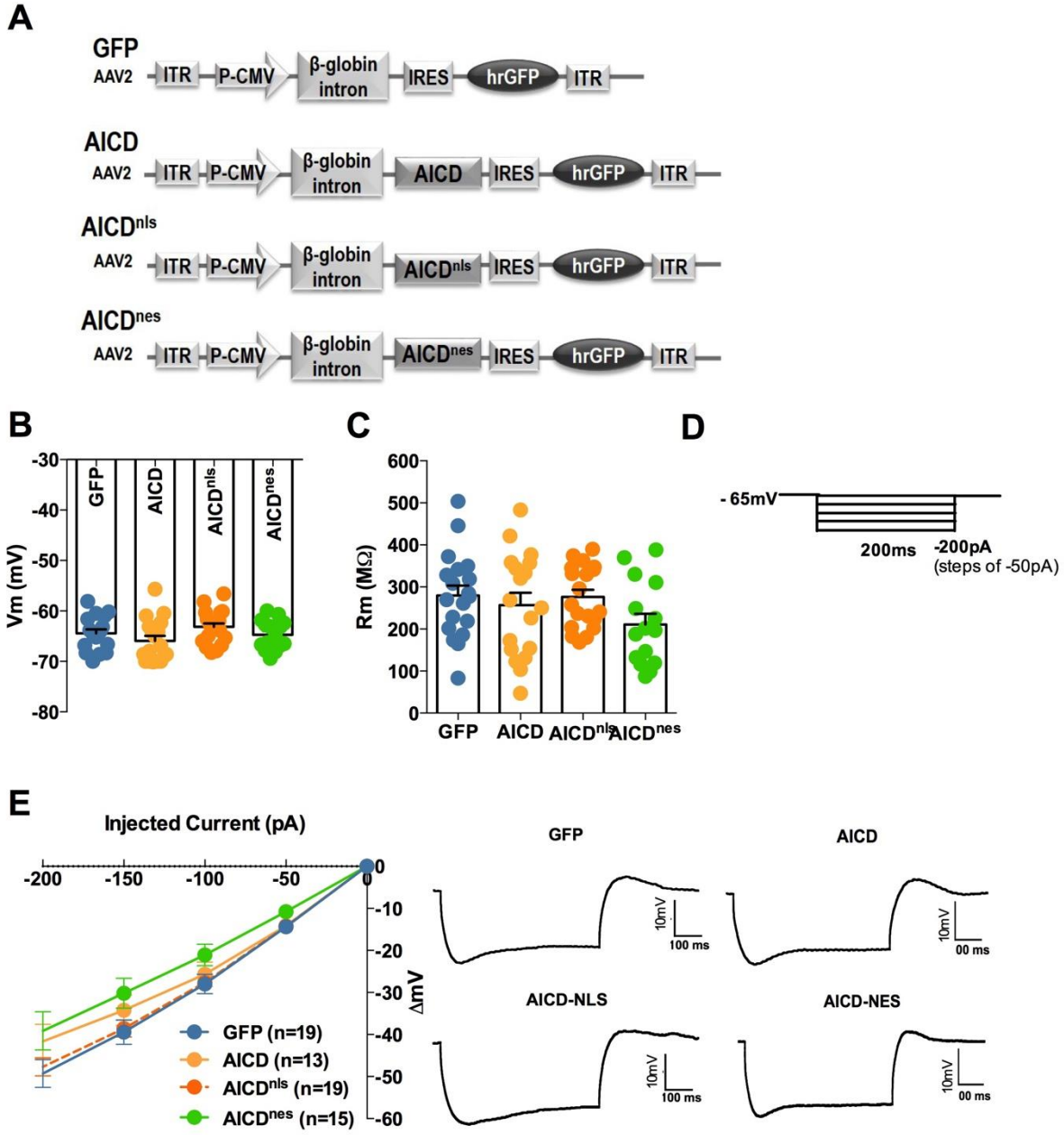

Figure S1 – Related to Figure 1. AICD does not modify neuron passive properties. (A) vector maps of the low-transduction efficiency AAV constructs used in this study. AAV constructs: AICD, $AICD^{nls}$ or $AICD^{nes}$ were inserted downstream of the CMV promoter and β-globin intron and upstream of an IRES-GFP sequence. ITR: inverted terminal repeats; P-CMV: cytomegalovirus promoter; IRES: internal ribosomal entry site; hrGFP: human recombinant green fluorescent protein. (B-C) Scatter dot plot graphs show in (B) the resting membrane potential (Vm) and in (C) the membrane resistance (Rm) of transduced neurons. Each dot represents one neuron. (D) Protocol used to assess the membrane resistance of CA1 pyramidal cells. 200 ms hyperpolarizing current pulses, incremented in steps of -50pA, were applied at a pre-stimulus potential fixed at -65 mV. (E) Steady state values of membrane hyperpolarization ($Vm-V_h$, where V_h= -65 mV) plotted vs. the negative current amplitude. On the right, traces of voltage responses to hyperpolarizing current step -100pA recorded from neurons transduced with the indicated virus. Statistic details are fully described in Supplemental Information Table S1.

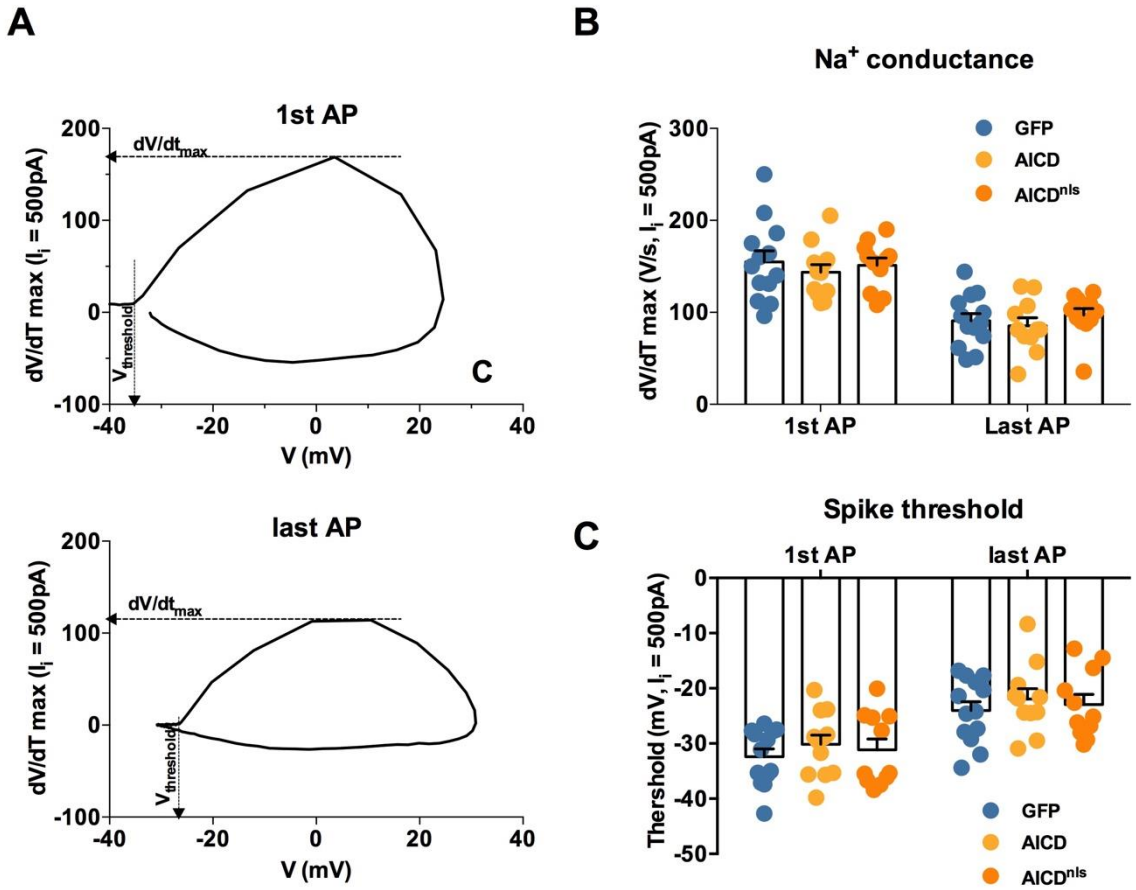

Figure S2 – Related to Figure 1. Na^+ channels responsible for AP generation are not implicated in the AICD-regulation of neuronal excitability. (A) Example of "Phase-plane plots" obtained by plotting dV/dt vs. voltage in a neuron transduced with GFP, considering the first and last APs of the train spike from trace shown in Figure 1E. (B) Scatter dot plot graphs show in (B) the dV/dtmax calculated from the "Phase plane plots" obtained from the AP trains induced by 500pA current step and in (C) the spike threshold values taken as 4% of dV/dtmax. Each dot in (B) and (C) represents one neuron. Statistic details are fully described in Supplemental Information Table S1.

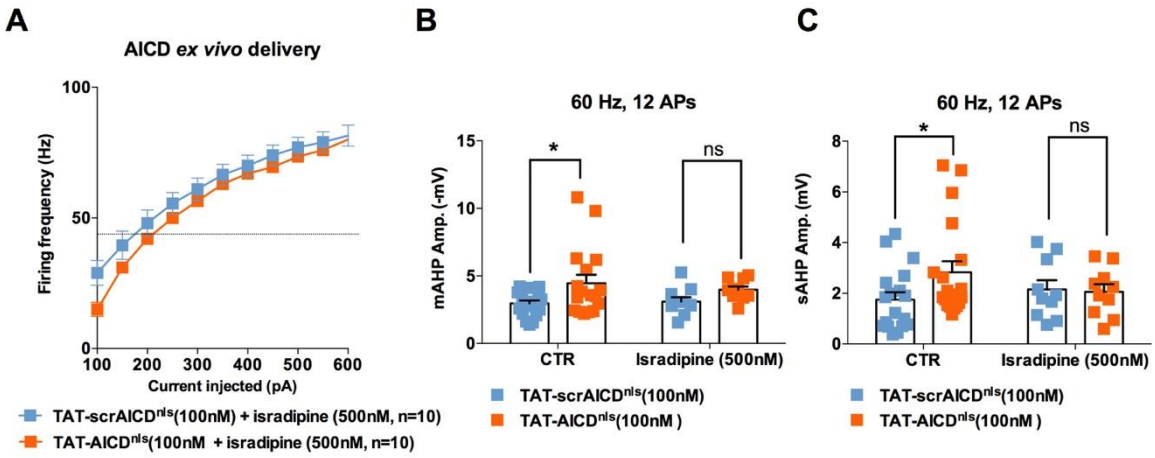

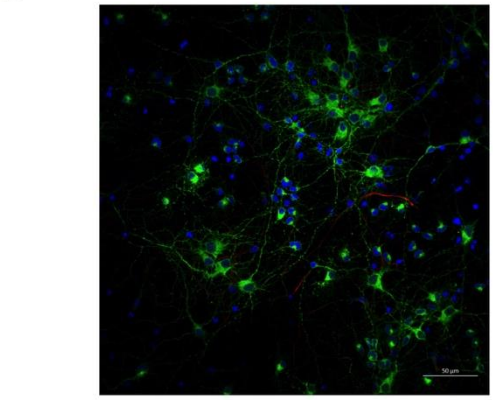

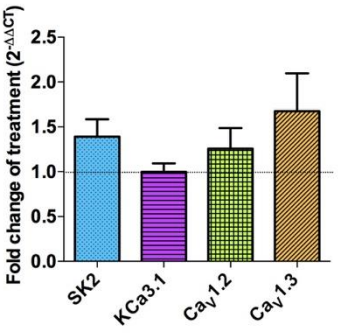

F

Primer	Target Gene	Organism	Forward Primer	Reverse Primer	Amplicon Size
CypA	PPIA peptidylprolyl isomerase A (cyclophilin A)	rat	TATCTGCACTGCCAAGACTGAGTG	CTTCTTGCTGGTCTTGCCATTCC	127bp
Rpl13A	Ribosomal protein L13A	rat	GGATCCCTCCACCCTATGACA	CTGGTACTTCCACCCGACCTC	131bp
KCCN2	Potassium Calcium-Activated Channel Subfamily N Member 2	rat	TATGCGCTCATCTTCGGCAT	AGAATACAGCGACGCCTTGT	93bp
KCNN4	Potassium Calcium-Activated Channel Subfamily N Member 4	rat	AGTGTTTAATCACGCTGTCCACT	CCCGTTGTCAGTCATGAACA	92bp
Cancna1c	Calcium voltage-gated channel subunit alpha1 C	rat	TGCCTCCGAACACTACAACC	CCCCGCACACAATGAAACAG	173bp
Cacna1d	Calcium voltage-gated channel subunit alpha1 D	rat	GAGGCCAAAAGTAACCCCGA	AAGTCGAGACCGTGAAGAGC	160bp

Figure S3 – Related to Figure 4. Effect of Isradipine on neuron excitability in control and AICD neurons and qPCR experiment to analyze levels of SK2, KCa3.1 and L-type calcium channels. (A) Mean firing frequency vs. injected current summary plot recorded in neurons from slices pre-incubated in TAT-scrAICD^{nls} and TAT-AICD^{nls} peptides (100nM) for 2h, and after recorded in the presence of the L-type Ca^{2+} channels blocker, isradipine (500 nM), in the bath perfusion. (B) and (C) Scatter dot plot graphs showing (B) mAHP and (C) sAHP amplitude (Vm-V_h, where V_h=-65mV) recorded from neurons submitted to a depolarization current step sufficient to induce a train of 12 APs at 60Hz. (D) Characterization of hippocampal primary neuronal cultures (15 days in vitro; MAP2 (neuronal marker), GFAP (astrocytic maker) and cell nuclei (scale bar - 50 μm), used to evaluate the effect of AICD on the transcription of putative targets: (E) qPCR results on genes coding for SK2 (*KCCN2*), KCa3.1 (*KCNN4*), CaV1.2 (*Cancna1c*) and CaV1.3 (*Cacna1d*) channels comparing control (TAT-scrAICD^{nls}) and treated (TAT-AICD^{nsl}) neurons. (F) Details of primers used for qPCR. (*P<0.05, Two-way ANOVA or Unpaired student-t Test). Each dot in (B) and (C) represents one neuron. Statistic details are fully described in Supplemental Information Table S4.

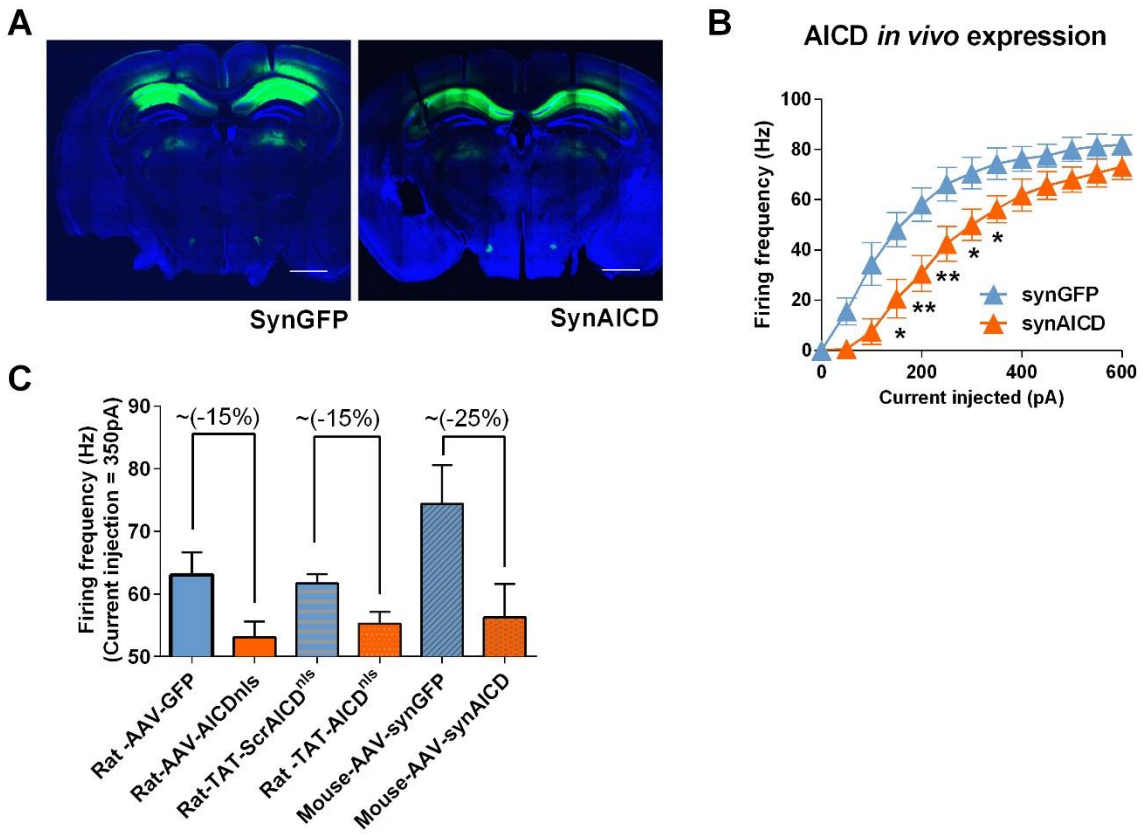

Figure S4 – Related to Figure 5. Comparison of AICD effect on neuron firing activity observed in the different experimental models. (A) Photos show representative images of coronal brain slices prepared from mice injected in vivo with synGFP and synAICD, as indicated. GFP and DAPI (nuclear marker). Images were acquired on the FV10 Olympus confocal microscope with automatized stitching. Scale bars 500 m. (B) Mean firing frequency vs. injected current summary plot recorded in neurons from mouse slices pre-incubated in TAT-scrAICDnls and TAT-AICDnls peptides (100nM) for 2h. (C) Bars graph showing AICD effects on neuron firing frequency observed in the different models. Statistic details are fully described in Supplemental Information Table S5.

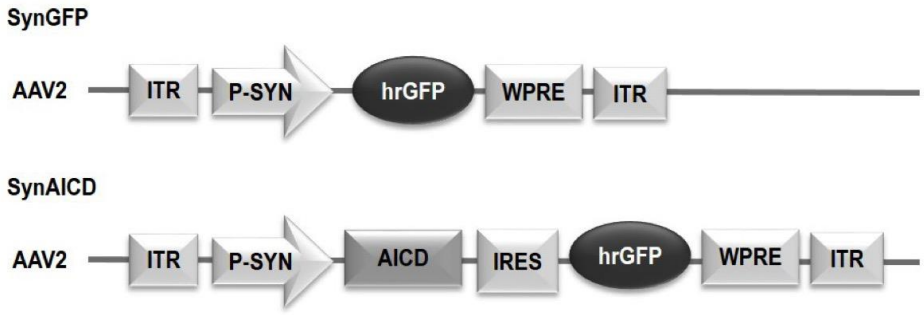

Figure S5 – Related to Figure 5 and 6. High titer SynAICD and SynGFP AAV constructs

Diagrams of AAV constructs representing SynGFP and SynAICD viruses, which exhibit specific expression of AICD in neurons with high transduction efficiencies. AICD was inserted downstream of the synapsin promoter and upstream of the hrGFP sequence via an IRES linker. ITR: inverted terminal repeats; P-SYN: synapsin promoter; IRES: internal ribosomal entry site; hrGFP: human recombinant green fluorescent protein; WPRE: Woodchuck Hepatitis Virus Post-transcriptional Regulatory Element.